Adv Polym Sci (2005) 182: 55–129
DOI 10.1007/b135560

Published online: 23 July 2005

Chemical Composition of Polymer Surfaces Imaged by Atomic Force Microscopy and Complementary Approaches

G. Julius Vancso (✉) · Henrik Hillborg · Holger Schönherr

MESA$^+$ Institute for Nanotechnology and Faculty of Science and Technology, Department of Materials Science and Technology of Polymers, University of Twente, P.O. Box 217, 7500 AE Enschede, The Netherlands
g.j.vancso@tnw.utwente.nl

Abstract In this article we review the recent developments in the field of high resolution lateral mapping of the surface chemical composition of polymers by atomic force microscopy (AFM) and other complementary imaging techniques. The different AFM approaches toward nanometer scale mapping with chemical sensitivity based on chemical force microscopy (CFM) are discussed as a means to unravel, for instance, the lateral distribution of surface chemistry, the stability of various types of functional groups in various environments, or the interactions with controlled functional groups at the tip surface. The applicability and current limitations of CFM, which allows one to image chemical functional group distributions with a resolution in principle down to the 10–20 nm scale, are critically discussed. In addition, complementary imaging techniques are briefly reviewed and compared to the AFM-based techniques. The complementary approaches comprise various spectroscopies (infrared and Raman), secondary ion mass spectrometry (SIMS), matrix-assisted laser desorption/ionization mass spectrometry (MALDI-MS), X-ray photoelectron spectroscopy (XPS or ESCA), and near-field optical techniques used for imaging.

1 Introduction

1.1 The Scope of Atomic Force Microscopy in Polymer Surface Characterization

The Atomic Force Microscope [1] with its various imaging modes, and the related Scanning Probe Microscopy techniques have changed the scientific landscape during the last 15 years. Atomic force microscopy (AFM) and related scanned probe techniques have become enabling methods (platforms) in cutting-edge nanotechnology. These instruments at the same time function also as a "workhorse" in scientific laboratories and are being used to assist solving materials science problems covering a wide range of issues. It is not the purpose of this review to introduce AFM, its operational principles, and the various imaging modes used in polymer research. Instead, the reader is referred to other reviews introducing AFM imaging [2–14], AFM-based studies, and force measurements using force-distance curves [15, 16].

We only mention here that the probe used in AFM is a sharp tip, which is attached to a flexible microbeam (microcantilever). In AFM various forms of interactions between the apex of the tip (with a radius between approximately 10–100 nm) and the sample surface are measured, either as a function of tip location with respect to the surface, or at a fixed (x, y) position as a function of the cantilever deflection or tip-sample distance. In most conventional instruments the cantilever-tip assembly is attached to a piezo controller, which positions the tip in the (x, y) scanned plane and adjusts the vertical position (piezo travel) to accommodate sample height, or to measure tip-sample force curves. The latest generation instruments can also be equipped with active x-y-z distance feedback control loops, which enable one to perform lithography, vertical positioning of the tip (e.g. for single molecule force spectroscopy), etc.

Whereas scanned probe techniques are being continuously developed, some applications have reached a relative maturity. At the beginning of AFM in the eighties emphasis in AFM-related research was put on surface topology imaging of structures from the 100 micrometer to the nanometer size domains. Distinct advantages of AFM, e.g., its capability to deliver "true" 3-D surface topology information, have been described in ample detail in the literature. A great deal of excitement was caused by nanometer-scale studies making use of the AFM's ability to visualize molecular packing in regular structures from a true nanometer scale perspective. Corresponding research was soon followed by work aiming at surface property studies on the nanoscale (tribology, adhesion by surface force measurements using AFM cantilevers as nanoscale force sensors, nanomechanics). With developments in imaging speed and stability, and with inventions enabling environmental control (temperature, imaging media, including gases and solvents) studies of processes (physical and chemical) and nanofabrication approaches are also gathering momentum (Fig. 1).

The chemical functionalization of AFM tips allows one, in principle, to map functional groups at surfaces, to pick up and deliver single molecule reactants, and to study force responses of (macro)molecules under mechanical tension, or exited by external fields (e.g. light). Various tip functionalization approaches have been described in the literature. By now, some of these can be considered as robust enough for being routinely used in research laboratory environments to study interaction forces between (functionalized) tips and sample surfaces in a simple manner. AFM tips with simple functional groups attached (e.g. in the form of a self-assembled monolayer of the functional molecules) can even be commercially purchased. The surface forces measured by AFM, of course, always include contributions by London dispersion forces. However, when functional groups are attached to tip surfaces, e.g., by AFM tip modifications, these can interact with surface groups via system-specific forces (H-bonding and other hydrophilic interactions, hydrophobic forces, acid/base type interactions, etc.) in addition to London

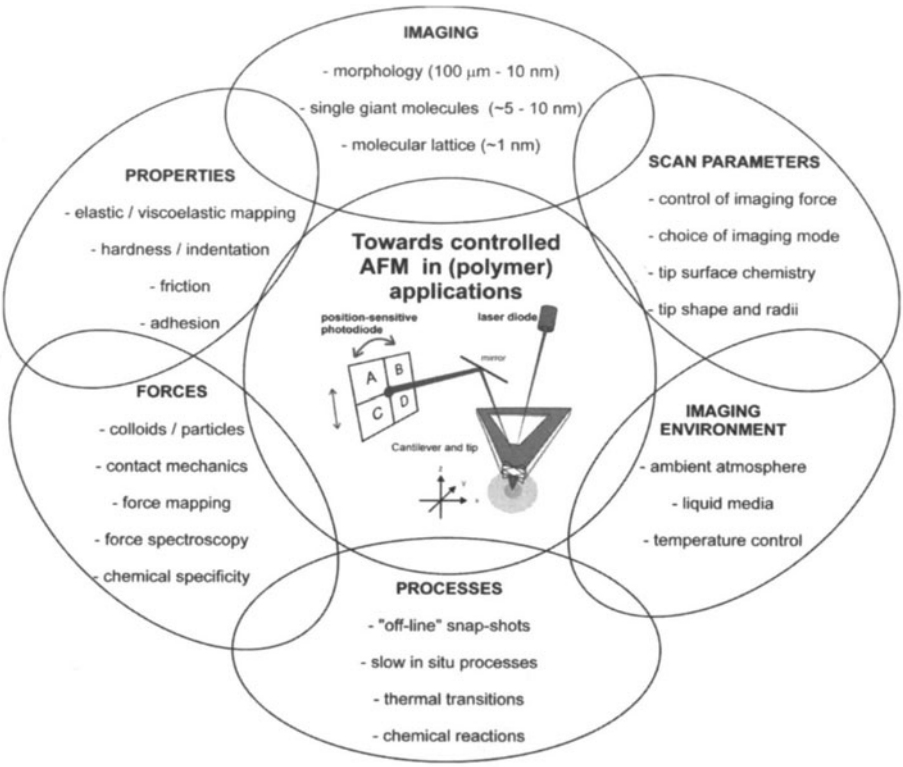

Fig. 1 Towards controlled AFM in (polymer) applications

forces. The tip force-distance curve characteristics measured reflect the sum of all of the specific and non-specific contributions.

As a result of the high lateral resolution of AFM when sharp probes and appropriate imaging conditions are used, in theory, lateral mapping of surface chemical groups can be performed with near nanometer (several tens of nm) resolution. This mapping involves measurements of the local variation of interaction forces either in the surface normal or in the surface tangential direction. Surface normal forces and forces at which AFM tips get disengaged in the surface normal direction give information about adherence,[1] while surface tangential forces are related to tribological properties (static and dynamic friction). By measuring local variations of normal and lateral forces, in ideal situations (for ideally smooth surfaces and without surface (visco)elastic deformation under the load of the AFM tip) one would image the lateral dis-

[1] We use here "adherence" to describe the practical work of adhesion to emphasize differences between its value and the magnitude of thermodynamic adhesion. The latter, if expressed in work of adhesion, corresponds to the reversible free energy change per unit surface area when two contacting surfaces are moved apart from contact to infinite distance of separation. Thus, adherence also includes the energy dissipated during separation of the contacting surfaces from each other.

tribution of chemical groups at the sample surface, hence the related method has been named "Chemical Force Microscopy" (CFM).[2] This nomenclature has been introduced by one of the first groups of authors [17] describing mapping of functional groups in self-assembled monolayes (SAMs) of end-functionalized alkanethiols. These authors mapped the spatial arrangement of different functional end groups exposed at the surface of the SAMs using chemically specific contrast between the tip and the SAM surface (see Sect. 5.1).

In this review we shall focus on "true" imaging with chemical sensitivity, with the main focus of using forms of AFM, which utilize and control chemically specific contrast between tip and sample, e.g., by controlled modification of the tip surface. AFM as a near-field technique has a limited field of depth, which can be significant (several tens of nanometers) only if soft, rubbery or viscoelastic polymers are studied. Hence, for smooth surfaces (i.e. without the perturbation of surface topological features and roughness) the interactions between tip and sample are dominated by the surface chemistry and surface mechanical properties. Thus, questions that one can raise regarding surface chemical composition include the lateral distribution of surface chemistry, the stability (e.g. for charged surfaces in electrolytes) of various types of functional groups in various environments, interactions with controlled functional groups at the tip surface, etc. CFM allows one to image chemical functional group distributions with a resolution, in principle, down to the 10–20 nm scale. However, chemical imaging is by no means routine, and one should carefully evaluate experimental strategies and data for lateral mapping of chemical groups. To this end, it is very essential to consider CFM as a complementary technique to the other surface imaging approaches, including spectroscopies (infrared – IR –, and Raman), secondary ion mass spectrometry (SIMS), X-ray photoelectron spectroscopy (XPS or ESCA), etc. Hence, these imaging techniques will also be reviewed in this article, albeit shortly, and differences and complementary approaches with CFM will be emphasized and discussed whenever appropriate.

Emphasis is laid in this review naturally on polymer specific problems. It is not our purpose to give a full encyclopedic account of the literature up to date. We shall rather focus on typical selected applications and introduce briefly the underlying physical and chemical concepts. We try to sketch the power and the limitations of CFM at the current state-of-the-art of the technological developments of CFM. The choice of the examples discussed reflects our preferences and scientific taste, but omissions may have also occurred by accident. We regret if we left out (by accident or by choice) articles from

[2] Chemical force microscopy (CFM) will be used as a synonym for "AFM using defined surface chemistry, for instance self-assembled monolayer functionalization, on AFM probe tips in order to measure differences in surface chemical composition" (using friction or adhesion differences related to interactions between functional groups or atoms exposed on both tip and sample surface as contrast) throughout this review article.

the literature which the corresponding authors would miss and we offer our apologies to those who consider these omissions as negligence on our part. We cannot provide justice to everyone.

1.2 The Case and Need of Surface Treatment of Polymers

In applications, such as coatings, adhesives and biomaterials, the surface properties, as well as good bulk mechanical properties, of polymers are equally important for their success. Since polymers often do not possess the required surface properties, various treatment techniques have been developed to modify their chemical or physical characteristics. Introducing functional groups, or modifying the surface morphology, for increased adhesion or decreased hydrophobicity are classical examples for these treatments. A limiting factor for biomaterials is, for example, non-specific protein interactions, often leading to undesirable responses from the host. These undesirable reactions are driven by surface-protein interactions. One method to enhance biocompatibility is by chemical modification of the surface by grafting biologically active molecules, such as peptides, proteins or polysaccharides. These surface modifications can be achieved by different techniques making use of either physical adsorption or covalent binding. Functional groups can be grafted by various techniques, such as plasma modification, gamma radiation grafting, photochemical reactions as well as exposure to oxidizing agents in solution.

With the recent development of various advanced surface characterization techniques, our understanding of polymer surfaces has been significantly improved, as well as our ability to control and even to tailor surface characteristics for specific applications down to sub-micrometer dimensions. Techniques for controlling the lateral distribution of functional groups on surfaces have a wide range of potential applications such as in biosensors, cell guidance, molecular electronics, wetting, membranes, etc. Regarding a general reference on polymer surfaces, the reader is referred to the book of Garbassi et al. [18]. Complementary microspectroscopic imaging is dealt with in the monograph of Koenig [19].

1.3 Homogeneous vs. Heterogeneous Distributions of Functional Groups at Surfaces

In thermodynamics of polymers (solutions, mixtures, etc.) radial pair distribution functions are of central importance as they contain information about the global character of intermolecular interactions and describe the structure on the atomic (segmental) ensemble level. Pair distribution functions and spatial distribution in heterogeneous (e.g. two component) systems

can also be statistically described and averages, such as preferential solvation and clustering, can be quantitatively derived. Once the pair distribution functions are known, average measurable thermodynamic quantities (derivatives of the corresponding thermodynamic potentials) can be calculated. Scattering experiments, as well as other thermodynamic measurements, such as "inverse" gas chromatography, can be used to derive statistical structure (and property) characteristics (see e.g. [20–23]). In principle, for heterogeneous surfaces similar surface-specific formalisms can be introduced. It has been recognized that surface chemical heterogeneities for multicomponent systems have a profound influence on surface-related phenomena, such as adsorption [24]. For a statistical description of surfaces, particle distribution functions should be specified to describe (average) values and distributions of surface-sensitive properties down to the characteristic observation depths from the (geometrical) surface into the bulk. Once the distribution function and the averaging processes (characteristic moments over the particle distribution functions) for the given property that depend on the spatial heterogeneity are known, the appropriate ensemble mean values (measurable) of the property in question can be derived. Although for the bulk such statistical treatments are standard, there is surprisingly very little described in the literature regarding statistical treatments of surface-related atomistic structures and properties (and related distributions). One important example is related to thermodynamic adsorption on heterogeneous surfaces, or interfaces. For heterogeneous surfaces [heterogeneous materials, surface treated (polymer) particles] adsorption sites can have different (free) energies and correspondingly a site energy distribution can be defined (and measured). For example, energy site distributions at the surface of xerographic toner particles (with heterogeneous average compositions) were characterized with success [21].

For heterogeneous surfaces in multicomponent systems it is surprising that virtually no quantitative description is usually given with respect to exact lateral distributions of surface (functional) groups down to quantity-dependent characteristic depths. One usually characterizes heterogeneous surfaces by number average concentrations of atoms or molecular fragments (XPS, SIMS) or patch sizes and shapes for surface phase-separated structures. For a quantitative description of surface structure and properties such distributions must eventually be introduced. However, there are only few experimental techniques, which give (in real space) adequate information about the atomic (or segmental) distribution of different species. Surface scattering (in Fourier space) could be used, but this falls beyond the scope of this review as we focus here on non-average local imaging of spatial heterogeneities of functional groups (in real space) and not on ensemble averaging. In the following sections it will become clear that a tremendous experimental and theoretical effort is needed until rigorous surface structure distributions for heterogeneous surfaces (and ultimately a first-principles based treatment of surfaces) can be given with atomistic details.

Polymer surfaces are often expected to show spatially heterogeneous distributions of functional groups as a result of, e.g., widely-applied surface treatment procedures and surface chemical reactions. The analysis of the spatially heterogeneous chemistry and the direct relation of this heterogeneous surface chemistry with related properties have been only recently addressed in detail. This lack of knowledge that we have just begun to overcome has been in part caused by the unavailability of suitable characterization tools that allow one to map the respective distributions on the sub 100 nm length scale.

The knowledge of the spatially heterogeneous distributions of functional groups is of widespread importance in polymer science and of striking relevance in the biochemical field. It is well known that, for instance, cell adhesion depends critically on the spacing of (poly)peptide sequences on functionalized substrates. For example, the effect of surface coverage of RGD protein sequences, which was at that time only indirectly related to lateral spacings, has been investigated in detail [25]. A minimum spacing of 440 nm was concluded to be necessary for spreading of cells, while focal point formation required minimal spacings of 140 nm. In an extension of this type of work, the direct control of spacing between adhesion islands was shown by Chen et al. to control cell growth or cell death [26]. More recently, the nanoscale clustering of RGD was unraveled [27], which clearly proves and exemplifies the importance of micro- and nanoscale analysis of the distribution of chemical functional groups at surfaces. Many of these and related biological and biochemical processes rely on biopolymers, such as proteins and peptides, in so far they can be considered part of polymer science. In addition, the interaction of man-made polymers and biological species is of crucial importance in for instance drug discovery and tissue engineering [28, 29], and hence the understanding of the underlying processes down to the molecular scale clearly requires advanced local chemically sensitive analysis and imaging methodologies, as discussed in this review.

In addition to the obvious impact of nanometer scale distributions of recognition units in controlling cell adhesion, the lateral heterogeneity of functional groups at polymer surfaces plays a centrally important role in many surface-related properties and processes, for example in the well-known phenomenon of wetting of surfaces. In most instances a liquid placed on a solid does not wet the surface, but remains as a drop having a definite angle of contact between the liquid and the solid phase. The idealized situation for a homogeneous, flat surface is illustrated in Fig. 2.

The contact angle θ is geometrically defined as the angle formed by the intersection of the two planes tangent to the liquid and solid interfaces at the perimeter of the contact between the two phases and the third surrounding phase, which is typically air or vapor. The change in surface free energy, ΔG, accompanying a small displacement of the liquid such that the change in area

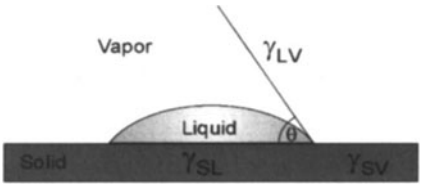

Fig. 2 Contact angle between a liquid placed on a solid surface and the surface; γ is the interfacial energy (or interfacial tension), and LV, SV, and SL in the subscripts refer to liquid-vapor, solid-vapor, and solid-liquid interfaces, respectively

of solid covered is ΔA, can be written as

$$\Delta G = \Delta A \left(\gamma_{SL} - \gamma_{SV}\right) + \Delta A \gamma_{LV} \cos(\theta - \Delta\theta) \tag{1}$$

where γ is the interfacial energy (or interfacial tension), and LV, SV, and SL refer to liquid-vapor, solid-vapor, and solid-liquid interfaces, respectively.

At equilibrium

$$\lim_{\Delta A \to 0} \frac{\Delta G}{\Delta A} = 0$$

and Eq. 1 becomes:

$$\gamma_{SV} - \gamma_{SL} = \gamma_{LV} \cos\theta \tag{2}$$

In combination with the definition of thermodynamic work of adhesion:

$$w_{SLV} = \gamma_{SV} + \gamma_{LV} - \gamma_{SL} \tag{3}$$

we can write Eq. 2 as

$$w_{SLV} = \gamma_{LV}(1 + \cos\theta) \tag{4}$$

Equation 2 was stated in quantitative form by Young in 1855 [30]; the equivalent (Eq. 4) was stated in algebraic form by Dupré in 1869 [31], along with the definition of work of adhesion.

By contrast, real surfaces can be rough and/or heterogeneous in composition [24]. In the following we will briefly discuss as an illustrative example how the wettability and the contact angles measured will depend on the surface composition. For instance, the surface can be composed by domains of different composition. The effect of a patchy structure on the Young equation was described by Cassie, who proposed the following equation (Cassie equation) for a two component, heterogeneous surface [32]:

$$\cos\theta = f_1 \cos\theta_1 + f_2 \cos\theta_2 \tag{5}$$

where f_1 and f_2 are the fraction of the surface having inherent contact angles θ_1 and θ_2. Equation 5 constitutes a simple arithmetic mean, weighted by the respective surface fractions of the components. The Cassie treatment of heterogeneous surfaces was reviewed by Israelachvili and Gee [33], who

modified Eq. 5 in order to account for heterogeneities close to atomic and molecular dimensions:

$$(1 + \cos\theta)^2 = f_1 \left(1 + \cos\theta_1\right)^2 + f_2 \left(1 + \cos\theta_2\right)^2 \quad (6)$$

Equation 6 replaces Eq. 5 whenever the sizes of the chemically heterogeneous patches approach molecular or atomic dimensions. In the latter treatment, polarizabilities, dipole moments and surface charges are averaged, owing to the very low dimension of heterogeneity, instead of cohesion energies as in the Cassie equation. Experiments on mixed monolayers of alkanethiols showed that the Cassie equation fits the variation of angle with surface fraction better than the Israelachvili–Gee equation [34], while for other systems the deviations were to within the experimental error [35]. While these treatments describe the effect of chemical composition on equilibrium contact angles, it is obvious that other techniques, in particular the imaging techniques discussed in this review, may provide differently weighted information.

Apart from wettability and the related spreading of liquids, chemically heterogeneous surface composition has a profound impact on adhesion and its respective failure mechanisms and defects [24]. Further relevant areas comprise release surfaces, corrosion, lubrication, as well as chemical surface functionalization in coatings, sensors and biomedical applications (stealth surfaces) [18]. These important phenomena together with related applications in miniaturized devices, where the tolerances for defects and lateral heterogeneities are rapidly decreasing, are in the focus of the microscopic techniques reviewed in this article.

An emerging area of applicability is the field of sub-micron and nanopatterning, where there is a clear need to analyze the chemical composition of patterns at the relevant length scales. Many of these applications are again ultimately located at the interface between polymer surface science and life science. For example, protein patterning of polymer surfaces via e-beam lithography [36], bioactive molecular patterning in the fabrication of biosensors [37] and high-throughput combinatorial chemistry analytical techniques [38], as well as light-directed, spatially addressable, stepwise chemical synthesis of bioactive biopeptides are target areas [39]. Other examples include applications in microfluidic devices for localized drug applications to cell cultures [40] and DNA analysis [41], and investigations on neuron networks [42, 43]. For fundamental understanding of these interface-related processes, knowledge on a sub-micrometer level is required.

In addition to the mentioned widespread phenomena related to polymer surface chemical composition, applications outside the life sciences are located e.g. in the area of semiconducting polymers [44], e.g. for the fabrication of polymeric light emitting diodes. For this particular topic, the efficiency of polymeric light emitting diodes has been shown to be dependent of the nucleation processes (referred to as nanometer-sized clusters) in conjugated polymer films. These phenomena can be successfully studied on

a sub-micrometer scale by a combination of Near-Field Scanning Optical Microscopy and AFM [45].

2 How can Polymer Surfaces be Modified?

The purpose of this chapter is to focus on controlled surface modifications of polymers, with emphasis on the advances achieved during the past decade or so. The commonly used techniques generally mentioned include corona discharge, plasma, UV, laser, and electron beam treatments. Lateral patterning techniques utilizing soft lithography, which is the collective name for a number of techniques where a patterned elastomer is used as mold, stamp or mask to generate or transfer patterns with sub-micrometer resolution, will not be covered in this chapter, since several comprehensive reviews focused on these techniques have been recently published [46, 47].

2.1 Plasma Treatment

The term "plasma" denotes a partially ionized gas containing a mixture of positive and negative charge carriers and neutral components. The overall charge of the plasma is neutral. Plasmas used for surface modification of polymers are generally not in a thermal equilibrium, but are generated by an external electric field applied over the gas mixture. This means that the gas temperature is usually hardly above room temperature even though the temperature of the electrons is much higher (10 000–100 000 K) and is only maintained as long as the external electric field exists. The reason for the low gas temperature is that the electrons make up only a very small part of all particles present and that the energies of positive ions and neutral species are only negligibly increased by the electric current within the plasma. By exposing a polymer surface to a plasma, it is exposed to this complex mixture of reactive species such as ions, electrons, as well as to UV radiation. Generally, the effects can be classified as follows [48]: (1) Surface reactions between gas-phase species and surface species introduce functional groups and crosslinks at the surface, (2) plasma polymerization, which involves the formation of a thin film via polymerization of an volatile organic monomer, and (3) etching, where materials are removed from the polymer surface by physical etching forming volatile by-products. There exists a large body of literature on surface modification of synthetic polymers by plasma treatments or plasma polymerization [49–55]. The advantage of the plasma processes is that the modification is limited to the top surface layer and does not affect the bulk properties of the polymer.

By using different types or mixtures of gases in the plasma, different surface functionalities can be obtained. Oxygen containing plasmas are the most frequently used treatments and these very effectively increase the surface energy of polymers by introduction of oxygen-containing species, such as hydroxyl, carbonyl, carboxyl and ether groups. Plasma treatments in noble gases, such as argon or helium, also result in a significant increase of oxygen containing groups. This is probably due to the exposure of the freshly treated, reactive surfaces to atmospheric oxygen after treatment or originates from trapped oxygen on the reactor walls [50] or oxygen dissolved within the polymer. Nitrogen containing plasmas can be used to introduce functionalities, such as amino groups. Fluorine containing plasmas are used to increase the hydrophobicity of polymer surfaces by the introduction of fluorine. Different functional groups can also be obtained by plasma polymerization using different monomers. For example, poly(ethyleneterephthalate) was functionalized in a glow discharge plasma by: $-OH$ (using allyl alcohol), $-NH_2$ (using allyl amine), $-CF_3$ (using perfluorohexene) and siloxyl groups (using hexadimethylsilane) [56].

Reports on the lateral distribution of the induced functional groups on polymer surfaces by plasma treatments have only been published recently. For example, using AFM with chemically functionalized tips, the lateral distribution of functional groups in plasma-polymerized allylamine films was investigated [57]. These measurements indicated the presence of a heterogeneous local environment of the amino groups formed, where patches exhibiting differences in hydrophobicity on a sub-50 nm scale were detected. In another study it has been shown that surface treatments of isotactic polypropylene with fluorine-containing gases resulted in an inhomogeneous distribution of the hydrophobicity on length scales below 50 nm [58].

Plasma-induced chemical micropatterning for cell growth is a new field of plasma surface modification of polymers. The advantages are the flexibility concerning type and density of introduced functional groups and the possibility to modify the morphology of the surface [59]. Moreover, the technique provides sterile surfaces and can be scaled to high outputs. Disadvantages are the low pressure and the UV-component which may cause denaturation and generation of multiple surface functionalities [59]. Another recent application of the plasma technique is mass production of disposable microfluidic devices by plasma etching (using an oxygen plasma) [60]. In most of these applications aiming at a lateral homogeneity of the introduced functionalities is obvious as is the need to develop suitable high resolution analysis methods.

2.2 UV-Radiation and UV-Laser Ablation

UV-radiation, generally in the range between 250–400 nm, can be used for lateral surface modification of polymer surfaces. The radiation causes

photon-activated fragmentation, or crosslinking, of the surface, where UV-sensitizers can be added to enhance the photon yield of the process. The characteristic penetration depth of the UV usually does not exceed a few hundred nanometers [61]. The technique can be used with lateral control of the functionalized groups using different atmospheres [62]. Polymer surfaces were irradiated by UV in different reactive gas atmospheres, where BrCN introduced nitrile functionalities, N_2H_4 introduced amino functionalities and $SO_2 + O_2$ introduced a mixture of thioureas and derivatives of sulfonic acids. Projection techniques allowed patterned modification of the surfaces to be made. Another application is improved micro-wear resistance of polymer surfaces [63]. Conducting patterns in 1-4-polybutadiene, doped by iodine, were made by UV-photolithography [64]. Conducting polymers are of interest for many potential applications in polymer batteries, integrated circuits, field-effect transistors, optical memory storage devices and electrochromic displays [65]. The microlithographic formation of conducting patterns is a key prerequisite for most of these applications [64].

UV lasers are photon sources characterized by energy and spatial coherence, whose energies can be in the watt range. The energies can be delivered in pulses and the narrow wavelength spread can be tuned to the maximum absorption of a polymer, making the treatments an energy-efficient process for patterning the surface. The photoablation process involves absorption of short-duration laser pulses, which excites and fragments the polymer chains. The resulting shock wave ejects the decomposed fragments (C_2, CO_2, CO) leaving behind a photoablated cavity [66]. Thus the method can be used as a dry etching technique. Special polymers, based on cinnamylidenemalonic acid ester groups, have been tailored for higher sensitivity to the laser ablation [67]. They exhibited high sensitivity, stability to wet etching (acids), high quality film formation properties and high resolution ablation structures. Prototyping can be performed using UV-laser ablation because of the flexibility of the direct writing [60]. A pulsed UV-excimer laser was used for photoablation of polymer surfaces, making fluid-handling microchannels with high aspect ratios for the fabrication of microdiagnostic devices [66, 68]. Bilayers of UV-absorbing and optically transparent polymer films were irradiated by UV-laser pulses. The UV-absorbing polymer was selectively photolyzed, and covalently crosslinked onto the transparent film. Fine surface patterns of the formed crosslinked film-layers were obtained by pulsed irradiation through a projection mask [69]. By using this method two dimensional patterns consisting of hydrophilic domains ($\approx 150\ \mu m \times 150\ \mu m$) of crosslinked poly(N,N-dimethylacrylamide) on hydrophobic polyethylene were created.

2.3 Electron/Ion Beam Treatment

Polymer surfaces can also be laterally modified using electron beam lithography. A focused beam of high-energy electrons is used to pattern a layer of electron-sensitive polymers, mostly poly(methyl methacrylate) [70]. By this process line widths < 5 nm have been achieved [71]. Using e-beam lithography, high resolution patterning of protein features on (poly(*tert*-butyl-methacrylate-*co*-methyl-methacrylate) with a resolution of 125 nm has been obtained [36]. Ion beams also contain high energy species, but these only affect the surface regions due to their higher mass. Ion beams are used in high-resolution patterning of polymeric surfaces, such as patterning of protein features on (poly(*tert*-butyl-methacrylate-*co*-methyl-methacrylate) [36]. Enhancement of interfacial adhesion between polypropylene and polyamide by functionalization of the polypropylene surface by low-energy ion beam irradiation has also been performed [72]. The modification depth was < 70 nm. Lithography with neutral metastable atoms has several advantages compared to electron and ion beams: thanks to the short wavelength (< 0.01 nm) the neutral beam can be focused to a spot that is limited by the size of one atom and the effects of diffraction will be very small even for lithography through masks with 10 nm scale features [73]. By exposing self-assembled monolayers (SAMs) on gold substrates to metastable argon atoms, the SAMs were sensitized to etching by an aqueous ferricyanide solution, which etched patterns into the gold.

2.4 Surface Grafting

Polymer surface grafting offers versatile means for surface modification. The advantages of the grafting technique are the easy and controllable introduction of new polymer chains with a high surface density and precise localization at the surface, while keeping the bulk properties unchanged [74]. If the surface to be modified possesses reactive groups, modification can be conducted by a chemical coupling reaction. If no functional groups are present they can be created by irradiation of the surface, generating radicals as surface sites for graft polymerization. Graft polymerization is usually achieved by the formation of highly reactive radical-generating species, such as trapped polymer radicals or peroxide groups, via γ-irradiation [75], UV irradiation [76–79], plasma, glow discharges or ozone treatments [53], followed by a subsequent radical polymerization at elevated temperatures in solution. By using tethered diblock copolymers (PS-*b*-PMMA), whose blocks can self-assemble, ordered arrays or patterns on the surface can be fabricated [80]. These nano patterns can be controlled by the degree of grafting, molecular weight of the blocks, volume fraction of diblock copolymer

and the Flory–Huggins interaction parameter [80, 81]. For example, well-defined poly(*tert*-butyl acrylate) brushes were prepared by a surface-initiated polymerization on silicon wafers [82]. The brushes were then patterned using photolithographic techniques yielding novel patterned polymer surfaces exhibiting well-defined hydrophobic and hydrophilic domains. Features as small as 1 μm could be reproducibly obtained [82]. Patterned polymer brushes of poly(caprolactone) were prepared from micro-contact printed gold surfaces. The key feature of this approach was to use the surface-initiated polymerization to chemically amplify the patterned SAM into a patterned macromolecular film. The benefit of this approach was the formation of patterned polymeric thin films without the need for photolithographic tools. This method is also tolerant to initial imperfections within the original monolayer structure [82].

Surface block-graft-copolymerization, based on the photochemistry of *N*, *N*-diethyldithiocarbamate has been applied to precisely design biocompatible and functional surfaces (patterns of immobilized heparin or proteins), as well as block-grafted surfaces on polystyrene [83]. Polystyrene surfaces have also been patterned by immobilization of poly(*N*-isopropylacrylamide) by photolithography, and subsequently used for regiospecific cell attachment [84]. Surface modification of polydimethylsiloxane microfluidic devices by UV induced polymer grafting improved the stability of the electroosmotic mobility and improved electrophoretic resolution of peptides [85].

2.5
Surface Patterns Originating from Physical Instabilities

Another class of methods for achieving patterning of polymer surfaces on a length scale of micrometers or less relies on a physical instability with an intrinsic length scale. Examples of such processes, which will not be further discussed in this review, include dewetting [86, 87], buckling produced by stresses arising from dispersion forces [88, 89] or residual mechanical stress [65]. Further approaches exploit the amplification of capillary waves by various means [90, 91].

3
Surface Tension and Surface Tension Models

In this section a brief introduction to the concept of surface tension and surface tension models for the determination of surface tension of solids is given. The surface tension (γ) is the tangential stress ($mN\,m^{-1}$) in the surface layer and is a direct measure of the intermolecular forces at the surface [92]. A number of empirical and semi empirical methods, based

on contact angle measurements, have been developed for determining surface tension of solids. Among these are the critical surface tension [93–95], the Good–Girifalco equation [96, 97], the equation of state by Wu [98, 99], Fowkes theory [100] and its extensions [101, 102], and Lewis acid/base interactions [103]. Controversies and discussions concerning the validity of these methods can be found in literature and have been reviewed by a number of authors [98, 104, 105].

3.1 Single Surface Tension Theories

The fundamental equation for the measurement of solid surface tension by using contact angle measurements is the Young's equation:

$$\gamma_{SV} - \gamma_{SL} = \gamma_{LV} \cos\theta \tag{7}$$

where γ_{SV}, γ_{SL} and γ_{LV} are the interfacial tensions between solid/vapor, solid/liquid and liquid/vapor respectively, and θ is the equilibrium contact angle. The γ_{SV} may be considerably less than the surface tension of the solid in vacuum (γ_S), as a result of absorption of vapor on the surface. The amount of reduction in the surface tension of the solid caused by this absorption is referred to as the equilibrium spreading pressure π_e:

$$\pi_e = \gamma_S - \gamma_{SV} \tag{8}$$

A stable equilibrium is obtained if the surface is ideally smooth, uniform and non-deformable. If the surface is rough or heterogeneous, the system may reside in one of many metastable states, and the measured angle is a metastable contact angle. In this instance, the contact angle is not only dependent of surface tension, but also on the surface roughness and the drop volume [98].

The concept of critical surface tension was proposed by Fox and Zisman [93–95]. An empirical, linear relation was found when plotting between the cosine of the advancing angle and the surface tension of a series of homologous liquids (referred to as a Zisman plot). The critical surface tension (γ_C) equals the surface tension of the liquid, when it is extrapolated to a zero contact angle on the solid:

$$\gamma_C = \lim_{\theta \to 0} \gamma_{LV} = \gamma_S - (\gamma_{SL} + \pi_e) \tag{9}$$

Since both the interfacial tension and spreading pressure will vary with the testing liquid, values of the critical surface tensions must be used with great caution [92, 98]. Non-linear relations are often observed if specific interactions (such as hydrogen bonding) between liquid and surface are present [94]. Moreover, it may not be sufficient to measure only the advancing angle, thereby losing information from the contact angle hysteresis [104].

Good et al. formulated a theory of interfacial tension between two phases using the geometric mean of the surface tension of each phase and suggested a general equation, known as the Good–Girifalco equation [96, 97]. When substituted into the Young's equation, neglecting the spreading pressure, this leads to [105]:

$$\gamma_{SV} = \gamma_{LV}(1 + \cos\theta)^2/4\Phi^2 \tag{10}$$

where Φ is an interaction parameter, characteristic of the molecular properties of a given system. The interaction parameter can be determined from a liquid homologue of the solid, or from molecular constants [98]. Based on the critical surface tension and the Good–Girifalco theory, Wu proposed an equation of state, which gives accurate values of surface tension [98, 99]. The contact angle of a series of testing liquids with known surface tension (γ_{LV}) is used to obtain a number of critical surface tensions ($\gamma_{C,\Phi}$).

$$\gamma_{C,\Phi} = \Phi^2\gamma_S - \pi_e = \frac{1}{4}(1 + \cos\theta)^2\gamma_{LV} \tag{11}$$

The $\gamma_{C,\Phi}$ is plotted against γ_{LV} to obtain a curve (the equation of state plot) whose maximum value ($\Phi \approx 1$) corresponds to the surface tension of the solid (γ_S). The maximum value is attained by matching the polarities of the testing liquids and the surface.

3.2 Theories Based on Multi-Component Surface Tension Models

These theories are based on the assumption that the surface tension can be considered as a sum of a number of independent components, each representing a particular intermolecular force [92]:

$$\gamma = \gamma^d + \gamma^p + \gamma^h + \gamma^i + \gamma^{ab} + \ldots \tag{12}$$

where $\gamma^d, \gamma^p, \gamma^h, \gamma^i$, and γ^{ab} are the contributions from London dispersion forces, polar forces, hydrogen-bonding forces, induction (Debye) forces and acid-base forces, respectively. Fowkes made the assumption that the surface tension was based on the sum of the hydrogen bonding and dispersive forces and derived an expression for the surface tension of a liquid on a solid in which only dispersion forces were common to both phases [100]:

$$\gamma_{SL} = \gamma_S + \gamma_L - 2\sqrt{\gamma_S^d\gamma_L^d} \tag{13}$$

This theory was then further complemented with polar contributions to the surface tension, for example by inserting the geometrical mean of polar components [101, 102] or by use of the reciprocals of the dispersive and polar surface tension components [106, 107]. Assuming that the geometrical mean could describe both polar and dispersion interactions Owens and

Wendt [102] proposed the following equation:

$$\gamma_{SL} = \gamma_{SV} + \gamma_{LV} - 2\sqrt{\gamma_{SV}^{d}\gamma_{LV}^{d}} - 2\sqrt{\gamma_{SV}^{p}\gamma_{LV}^{p}} \tag{14}$$

By inserting γ_{SL} into the Young's equation the two unknown solid surface tension components can be obtained via the measurement of the equilibrium contact angles of two liquids of known surface tension components, for example by using water and diiodomethane [102]:

$$1 + \cos\theta = 2\sqrt{\gamma_S^d}\left(\frac{\sqrt{\gamma_L^d}}{\gamma_{LV}}\right) + 2\sqrt{\gamma_S^h}\left(\frac{\sqrt{\gamma_L^h}}{\gamma_{LV}}\right) \tag{15}$$

Van Oss et al. [103, 108, 109] combined γ^d, γ^p and γ^i into a single component, which they called the apolar or Lifshitz-van der Waals component (γ^{LW}). The hydrogen bond (γ^h) and acid-base (γ^{ab}) components were described by electron acceptor-electron donor (Lewis acid/base) interactions of the polar component (γ_i^{AB}). The electron acceptor-electron donor parameters of the surface tension of a compound i are expressed as γ_i^+ (acidic term) and γ_i^- (basic term) according to: $\gamma_i^{AB} = \sqrt{\gamma_i^+\gamma_i^-}$ [108, 109]. The total surface tension is then obtained by the addition of the apolar and polar components. By combining this approach with the Young–Dupré equation the following equation is obtained [108]:

$$\gamma^{tot} = \gamma^{LW} + \gamma^{AB} = (1 + \cos\theta)\gamma_L = 2\left(\sqrt{\gamma_S^{LW}\gamma_L^{LW}} + \sqrt{\gamma_S^+\gamma_L^-} + \sqrt{\gamma_S^-\gamma_L^+}\right) \tag{16}$$

Thus by contact angle measurements using three different liquids (L), of which two must be polar, with known $\gamma_L^{LW}, \gamma_L^+$, and γ_L^- values, the $\gamma_S^{LW}, \gamma_S^+$ and γ_S^- of any solid (S) can, in principle, be determined. The value of γ_L must be known or determined independently [108]. The apolar component of the surface tension of solids (γ_S^{LW}) can be determined by contact angle measurements using strictly apolar liquids for which $\gamma_L = \gamma_L^{LW}$. These surface tension components can be related to experimentally determined pull-off forces between chemically modified AFM tips and an oxyfluorinated isotactic polypropylene surface in CFM approaches [110]. It was observed that the pull-off force measured with carboxylic acid tips in ethanol depended linearly on the basic term of the surface tension (γ_i^-) on the modified polymer surface.

3.3 Contact Angle Hysteresis

The most commonly used method for the determination of surface tension of polymers is the sessile drop technique. A droplet of a purified liquid is placed on a surface using a syringe. The angle formed by adding liquid to the

droplet, causing it to advance over the surface is termed the advancing contact angle. The angle formed by removing liquid from the droplet, causing it to recede over the surface, is termed the receding contact angle. The difference between the advancing and the receding contact angles is referred to as the contact angle hysteresis. Its value depends on the surface roughness and the surface heterogeneity [98]. Generally, the influence of the surface roughness on contact angle hysteresis is insignificant if the asperities are $< 0.5\,\mu m$ or if heterogeneous phases present with characteristic dimensions in the range of $< 0.15\,\mu m$ [98]. Cosines of equilibrium contact angles ($\cos\theta$) of liquids on heterogeneous surfaces with well-defined surface regions obey the Cassie equation which predicts a linear dependence on the surface composition, as mentioned previously (Eq. 5) [32].

Agreement with the Cassie equation has been obtained for contact angle measurements on surfaces micropatterned using $-CH_3$ and $-COOH$ groups [111]. Johnson and Dettre performed a theoretical analysis of a two-region surface consisting of circular, low ($\theta_1 = 120°$) and high ($\theta_2 = 0°$) surface energy regions, ranging between 100 to 25 μm in diameter [112]. They found that the advancing angles were associated with the low-surface-energy regions, whereas the receding angles were associated with the high-surface-energy regions. Furthermore, the contact angle hysteresis was found to increase with decreasing diameter of the phases. They concluded that both the advancing and receding angles must be measured to obtain reliable data describing surface heterogeneities [112]. Other phenomena that may cause a contact angle hysteresis on polymer surfaces include the dynamic nature of the polymer network (reorientation of functional groups) [53, 104] or swelling and liquid penetration by the probing liquid [18]. Critical measurements of the contact angle hysteresis and its time dependence offer a valuable help to understand the nature of polymer surfaces, especially in combination with other surface sensitive techniques [104].

4
Techniques to Measure Ensemble Average Distributions

4.1
Surface Forces

The chemical nature of surfaces determines most of their characteristics such as surface tension and adhesion. In the previous Section we discussed the basic definitions and experimental techniques for studies of surface tension in polymer systems. We have seen that the outmost atomic layers with a characteristic action radius determine the magnitude of the various components of the different types of interactions, which contribute to the excess free energy

of surfaces. A typical atom in the bulk is surrounded by its neighbors and experiences forces in all directions due to interatomic (chemically specific) interactions. The resulting interatomic force fluctuates in equilibrium (without additional external forces) around a zero value. In contrast, if atoms (or other specii) are at the geometrical surface of the body under consideration, they are only interacting by the atoms below or beside them (disregarding the gas and vapor molecules present above the surface). The net resulting force is pointing towards the interior and its value depends on pair- and multiatomic forces within an action radius. Whereas the first neighbors make the strongest contributions, there are non-zero force contributions also from the second, third, etc. coordination spheres below the particular surface atom being considered. These make an effective contribution to surface forces (hence to surface tension) up to a characteristic distance of a few atomic (molecular) layers. Thus macroscopic surface tension techniques result in values averaged over a characteristic action radius with a typical value in the range of up to a few nanometers. In addition, for multicomponent systems (with different atoms and molecules) all the different pairs of the mixed type interactions contribute to macroscopic surface tension. Hence these techniques average over chemical composition, as well as the characteristic action radius of the corresponding surface forces.

Differences in surface tension (surface free energy) and in adhesion for different substances are a result of different interatomic (intermolecular) forces. These (surface) forces are also responsible for the work required when two contacting bodies are separated from contact to infinite distance. Although the physical origin of all relevant intermolecular forces from a physical chemistry point of view stems from electromagnetic interactions, it is customary to group these in categories based on characteristic phenomena which dominate the essential physical behavior. Thus one speaks of ionic (monopole), dipole-dipole, ion-dipole interactions, induced dipolar forces, van der Waals (London dispersive) interactions, hydrophobic and hydrophilic, solvation, structural, and hydration forces, steric and fluctuation forces, etc. The reader finds an in-depth description and review of all these interactions in the book of Israelachvili [113]. Disregarding London dispersive forces, in cases when forces between a pair of complementary specii depend on the choice and the nature of these, one speaks of specific (molecule-specific) interactions. For example, strong dipole-dipole interactions occur when a hydrogen atom bonded to an electronegative atom in a given molecule interacts with the lone electron pair of a nearby electronegative atom, bonded in another molecule. The complementarity here is obvious such as in ligand-receptor (key-lock), or antibody-antigen type interactions for entirely specific pairs that bind together in biological molecules (e.g. for biotin and avidin, with an interaction energy of 35 kT which is one of the highest known for ligand-receptor systems) [113]. It should be mentioned that for H-bonded and some other

ligand-receptor pairs the term specificity does not always mean exclusivity for the choice of a given pair (no obvious need for a geometrical fit).

For polymer surface properties controlled by the chemical composition, thermodynamic (equilibrium), non-equilibrium, and technical terms and definitions play an important role. These are not always used in a consistent way, hence a short recapitulation seems appropriate. The thermodynamic work of adhesion (W_A) is defined as the reversible work (the free energy change) required to separate two phases with unit area of contact, from contact to infinity. The corresponding work of adhesion (and cohesion for similar bodies) can be easily expressed with surface tension values. In general, for surfaces of two intimately contacting solids ("1"and "2", respectively) each with a unit area, are separated in a medium ("3"), a work W_{132} is required which can be expressed as:

$$W_{132} = W_{12} + W_{33} - W_{13} - W_{23} \tag{17}$$

This equation is easy to understand as one new 1–3 and one new 2–3 unit surface areas are created at the expense of breaking up the unit area 1–2 contact and expanding the fluid by two unit areas to cover both sides of the originally contacting bodies. This expression is valid for processes that occur through quasi-equilibrium steps, i.e. when energy dissipation (e.g. due to surface or interface molecular relaxation and other processes) is negligible. This is, however, often not the case, i.e. net rearrangements of surface-proximity atoms, groups of atoms or molecules accompany approach or withdrawal. In addition, stored elastic energy (due to molecular stress fields) will also relax and gets dissipated by internal atomic and molecular scale friction. These dissipative processes, i.e. surface molecular rearrangements and internal stress relaxation give rise to differences in adhesion for outbound and inbound movement cycles and result in hysteretic behavior. Further contributions to dissipative processes can originate in surface topology (e.g. roughness) effects. Adherence is experimentally easier to access (as opposed to adhesion) and is used to describe the energy required to separate the two contacting surfaces during a mechanical test. The value of adherence (which can be determined by specific experimental techniques) is usually greater that the (presumed) value of adhesion e.g. due to contributions by viscoelastic dissipation, plastic deformation and other forms of dissipated energy [114].

The basic concept in chemical force microscopy is to scan forces of adherence, from pixel to pixel in AFM experiments with chemically specific contrast. As force in general is a vectorial quantity, for a full characterization its magnitude and direction are both needed. However, in AFM instead of fully measuring both, the lateral and the normal components are separately recorded. Here we assume the usual measurement geometry i.e. the sample surface being horizontal, and the AFM tip mounted above the specimen (with a cantilever long axis making a shallow angle with the sample surface). The magnitude of the lateral component, i.e. the friction force, de-

pends on the normal load. The normal (vertical) component is the sum of the vertical (pre-set) load (which can be positive upon pushing the tip into the sample, or negative, upon pulling the tip away from the surface) and the normal component of the surface (adhesion) and elastic (deformation) forces, respectively. As discussed in section 5, during a tip-sample approach cycle at snap-on the tip jumps in contact as the gradient of attractive forces overcomes the cantilever spring constant and the magnitude of the net attractive normal forces (including the elastic bending force of the cantilever) becomes negative at a characteristic tip-sample distance. The opposite happens at withdrawal when at increasing piezo displacement (thus increasing bending of the cantilever-spring and increasing negative normal force) the tip jumps out of contact. This pull-off happens when the cantilever spring constant overcomes the gradient of attractive forces and the total force on the tip (surface, adhesion, and tip-elastic contributions) crosses zero and becomes positive. At this point the tip jumps out of contact. The magnitude of the snap-on (pull-on) and pull-off forces are usually different as the sample-cantilever tip mechanical system is bistable and exhibits an inherent hysteresis loop. This hysteresis and the basics of lever mechanics, lever-tip sample contact and non-contact interactions are nicely described by Sarid in one of the first reference books on AFM [5]. It should be mentioned that the lever hysteresis and the adhesion hysteresis have different origins; i.e. lever hysteresis can be present for ideal, non-dissipative sample-tip systems, as well.

For imaging with chemical sensitivity (either based on adhesion, or on friction force contrast arising from chemical composition differences) it is relevant to understand the physical origins of the pull-off forces. Naturally, during an AFM force-distance cycle, a contact between tip and sample (in general, within a medium, e.g. in a fluid cell) is first established during approach and then broken during withdrawal. The radius of the contact areas between AFM tip and sample are small (typically in the range of tip radii of several tens of nanometers for imaging i.e. low normal force conditions). It is of interest to consider theories of (continuum) contact mechanics as starting point which quantitatively describe the pull-on and pull-off forces and related work of adhesion. It is also of interest to consider whether the corresponding macroscopic contact mechanics theories break down at the level of only a few contacting (effectively interacting) pairs of atoms (or molecules) in AFM. Another reason for discussing adhesion is due to interrelations between friction and adhesion. In friction force microscopy (sometimes referred to as Lateral Force Microscopy) forces of friction (lateral forces) are measured by detecting the torsion of AFM cantilevers. Intuitively, one anticipates correlations between adhesion and friction as surface forces are being broken (and formed) during both processes. Related studies e.g. by the surface forces apparatus (SFA) [115, 116] showed that the static friction force to start a sliding motion is related to the thermodynamic work of adhesion. However, kinetic

friction also depends on the irreversible component (i.e. energy dissipation) of the adhesion work. Hence, adhesion hysteresis (which can be measured e.g. in contact mechanics cycles) yields information about kinetic friction.

We summarize below the most relevant results of contact mechanics theories due to their relevance for AFM adhesion (and thus chemical mapping) research.

4.2 Adhesion Force and Work of Adhesion between Solids

The physical foundation of any treatment dealing with adhesion and friction forces is the knowledge of interatomic (intermolecular) potentials. If the pairwise (two-body) potential between two specii is described by a potential $V(r)$ as a function of the distance, r, between the particles, the force $F(r)$ and the potential are related through simple differential (integral) equations:

$$-F(r) = \frac{\mathrm{d}V(r)}{\mathrm{d}r} \tag{18}$$

$$V(r) = -\int_{r}^{\infty} F(r')\,\mathrm{d}r' = \int_{\infty}^{r} F(r')\,\mathrm{d}r' \tag{19}$$

The potential energy for a pair of atoms at a separation distance of r can be obtained as the integral (area) under the force-distance curve between infinity and the distance r (see Fig. 3).

The pairwise potential energy $V(r)$ between two non-bonded intermolecular pairs (strictly speaking atoms) as a function of intermolecular separation, r, can be obtained by summing repulsive and attractive potentials which are often approximated by the "6–12" Lennard–Jones potential:

$$V(r) = 4\varepsilon\left[\left(\frac{\sigma}{r}\right)^{12} - \left(\frac{\sigma}{r}\right)^{6}\right] \tag{20}$$

where σ is the equilibrium intermolecular separation and ε is the depth of the potential well at equilibrium separation (see Fig. 3).

The values of the power exponents can differ from "6–12" for various cases (see reference [113]); for example for H-bonded systems a "12–10" potential gives a better description. Various other functional forms are used to describe the pairwise potential energy, for details the reader is referred to the literature.

For van der Waals potentials the values of the two parameters, i.e. σ and ε, must be known. If the concrete forms of the interatomic potential functions (including all different types of London dispersion, dipole, induced dipole, etc. forces) are known, the usual treatment of calculating net forces between objects includes a "pairwise" summation of the interaction forces between atoms (molecules). Here we neglect multibody interactions, which can be

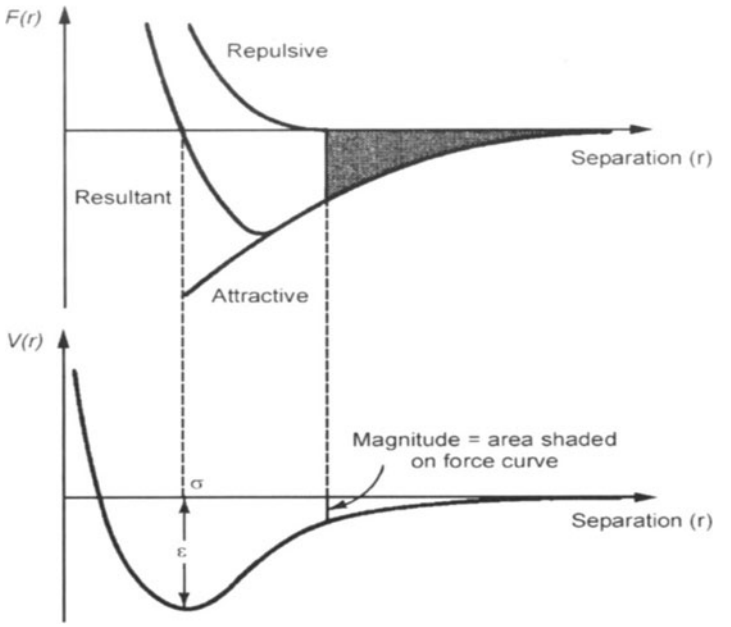

Fig. 3 Potential energy $V(r)$ and force $F(r)$ for two interacting atoms ("point-like" molecules) as a function of separation distance r

considered, e.g. by Green-function formalisms. Additivity is assumed during calculations of pairwise interactions and retardation effects for interactions are usually neglected. In addition to the knowledge of the two-body interaction potential energy functions, the exact geometry of the interacting bodies (e.g. sphere and a semi-infinite planar object) must also be known. The corresponding so-called Hamaker summation method [113, 117] is well described in texts and references and also in AFM-related references [5]. Regarding the interaction energy $W(d)$ of a sphere with a semi-infinite planar object made of two different types of materials (i.e. having the number density of atoms "ϱ_1" and "ϱ_2", respectively), it has the following form as a function of gap distance "d" between the sphere and the flat:

$$W(d) = -\frac{AR}{6d} \tag{21}$$

where R is the radius of the sphere and "A" is the Hamaker constant defined as:

$$A = \pi^2 C \varrho_1 \varrho_2 \tag{22}$$

keeping only the attractive part of the van der Waals potential $w(r) = -C/r^6$ ($C = 4\varepsilon\sigma$) between the corresponding pairs of atoms of the sphere and the semi-infinite flat, respectively. In Figs. 4 and 5 we depict typical examples of

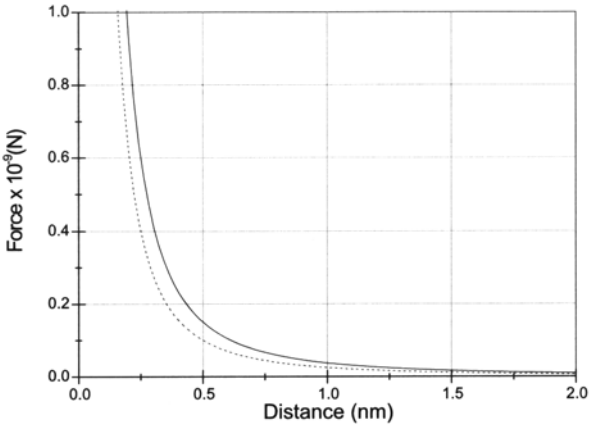

Fig. 4 Intermolecular forces vs. distance between a sphere (with a radius of 50 nm) and flat surfaces. *Solid curve*: both sphere and planar surface are terminated by hydrocarbon groups across water as a medium, with a Hamaker constant of 4.5×10^{-21} J ([113], pg 189). *Dashed curve*: both sphere and planar surface are modified with bilayer surfaces composed of the uncharged sugar-headgroup lipid, monogalactosyl diglyceride in 0.15 M NaCl, with a Hamaker constant of 3.5×10^{-21} J ([113], pg 396) (source: Zou S., private communication)

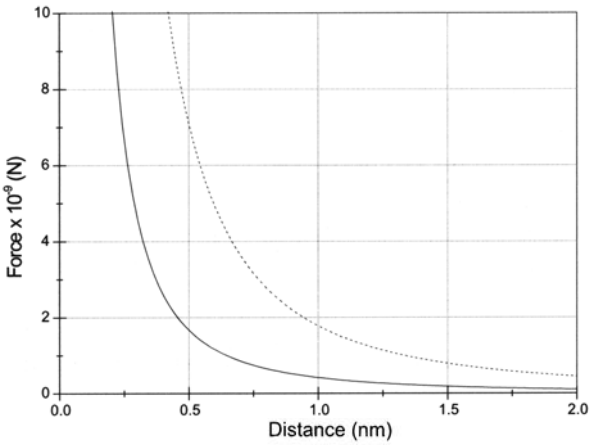

Fig. 5 Intermolecular forces vs. distance between a sphere (with a radius of 50 nm) and flat surfaces. *Solid curve*: both sphere and planar surface are terminated by hydrocarbon groups across vacuum as a medium, with a Hamaker constant of 0.5×10^{-19} J ([113], p 178). *Dashed curve*: silicon nitride/silicon scenario, with a Hamaker constant of 2.13×10^{-19} J [118] (source: Zou S., private communication)

the van der Waals forces for different surfaces as a function of separation distance in different media.

Interactions between atoms and molecules are usually described by potential energies as a function of separation distance as the directly measured

quantities are usually of thermodynamic nature. In force microscopy the negative differential of the potential energy function, i.e. force-distance – is measured, hence we should now relate force and potential. For two general curved surfaces with radii of curvature R_1 and R_2 the force $F(D)$ as a function of distance of separation, D, is related to the energy per unit area of two planar surfaces at the same separation (Derjaguin approximation, Israelachvili) [113]:

$$F(D) \approx 2\pi \left(\frac{R_1 R_2}{R_1 + R_2} \right) W(D) \tag{23}$$

The most useful consequence of the Derjaguin approximation is that it allows one to obtain a force law (by considering local curvatures of any curved surface) for any given geometry of two interacting bodies. If the work of adhesion between two bodies (in a third medium) is given by W_{132} then the adhesion force between two infinitely stiff (non-deformable) spheres of respective radii of curvature R_1 and R_2 of the given materials has the following form:

$$F = 2\pi \left(\frac{R_1 R_2}{R_1 + R_2} \right) W_{132} \tag{24}$$

Upon approach (or withdrawal) of objects surface forces can be determined (surface forces apparatus, AFM). To estimate forces for a typical AFM experiment, let us consider a sphere with a radius of 1 μm (replacing an AFM probe) at a distance of 1 nm from a surface. A characteristic value of the constant $C = 4\sigma\varepsilon = 5 \times 10^{-78}$ Jm^6 with $\varrho_1 = \varrho_2 = 3 \times 10^{28}$ m^{-3}. In this case a Hamaker constant $A = 1 \times 10^{-19}$ J was used and the corresponding force obtained had a value of 1.6×10^{-8} N (16 nN). In reality, the tip radii of AFM probes are much smaller (on the order of 10–20 nm) and the tip-sample distance varies depending on AFM operating conditions. Typical values of contact forces (at pull-off) in characteristic AFM experiments are in the range of 10 pN–10 nN.

Infinitely stiff spheres do not deform when brought in contact and pressed together. Hence the contact between them is a point contact. If the Young's modulus of the contacting spheres is finite, then the contact point becomes a contact circle with a radius "a". The value of the contact radius "a" depends in such cases on the elastic properties of the spheres, on the Young's moduli E_1 and E_2, and on the Poisson's ratios ν_1 and ν_2, of the two contacting materials, respectively. The value of the contact radius "a" can be calculated from the following formula:

$$a^3 = \frac{3}{4} \left(\frac{1 - \nu_1^2}{E_1} + \frac{1 - \nu_2^2}{E_2} \right) \frac{R_1 R_2}{R_1 + R_2} L \tag{25}$$

with the load L pressing the two spheres together. For this simplest case no surface forces were assumed, and the "flattening out" of the contact area from a geometrical point to a circle is fully due to elastic deformation under

load. The corresponding expressions were derived by Hertz, hence the name "Hertzian contact". Naturally, if one of the surfaces (say R_1) is planar, then $R_1 = \infty$ and $R_2 = R$; or if one of the surfaces is rigid $E_1 = \infty$ and $E_2 = E$. If the contacting sphere is rigid (stiff AFM tip pressing against an elastic, planar surface) then the contact radius is written:

$$a^3 = \frac{3}{4}\left(1 - \nu^2\right)\frac{RL}{E} \tag{26}$$

However, when surface (adhesive) forces are present, the shape of the contacting spheres in the vicinity of the rim of the contact area will further be deformed. Due to van der Waals attraction, this additional deformation of the elastic body will pull the two contacting objects closer together and hence further increases the contact radius with regard to the Hertzian value.

It was Johnson, Kendall and Roberts (JKR) who described the area of contact of two spheres including surface energy under the combined external load and the load of adhesion forces [119]. Figure 6 shows the contacting geometry for an infinitely stiff (rigid) surface and an elastic sphere for the Hertzian (dashed line) and JKR (solid line) contacts, respectively. Near the contact the vertical arrows at the dashed contour represent the surface forces which cause an additional deformation of the elastic sphere thus increasing the contact radius from a_H (Hertz) to a_{JKR} (JKR). The contact radius for the JKR model is a function of the external load, the work of adhesion, the radius

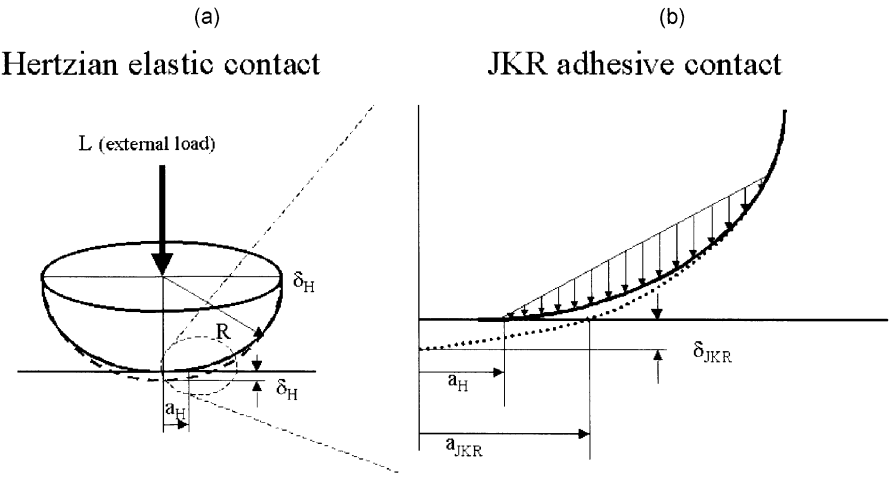

Fig. 6 Comparison of elastic Hertzian contact (*left*) and adhesive JKR contact (*right*). (**a**) Hertzian contact: *Dashed line* (sphere): shape of contacting spherical lens prior to pressing to the flat by force *L*. Hertzian contact profile shown by *solid line*, with radius under external load L : a_H; (**b**) JKR contact: Schematic of adhesion force (adhesive "zone" model, forces schematically indicated by vectors) further deforming a spherical lens from Hertzian contact (*solid line*) to JKR contact (*dotted line*) with radius a_{JKR}

of the contacting sphere (or if two different spheres are contacting, the reduced radii) and the elastic constant K (a combination of the Young's moduli and the Poisson's ratios of the contacting materials), defined as:

$$\frac{1}{K} = \frac{3}{4}\left(\frac{1-\nu_1^2}{E_1} + \frac{1-\nu_2^2}{E_2}\right) \tag{27}$$

written as:

$$a_{JKR}^3 = \frac{R}{K}\left[L + 3\pi W_{123}R + \left(6\pi W_{123}RL + \left(3W_{123}\pi R\right)^2\right)^{\frac{1}{2}}\right] \tag{28}$$

The value of a_{JKR}^3 can only become zero (at rupture of contact) if the normal force is negative, i.e. if the contacting sphere is pulled up (away from the flat). If this is the case, a physical solution can only exist if

$$6\pi W_{132}RL \leq \left(3W_{132}\pi R\right)^2 \tag{29}$$

When the contacting sphere is about to "jump off", the force that is necessary to separate the sphere from the flat plane, L_{pf}, is written as

$$L_{\mathrm{pf}} = -\frac{3}{2}\left(W_{132}\pi R\right) \tag{30}$$

For the Hertzian contact no force is needed to pull away the contacting sphere from the flat plane in excess of the weight of the sphere. However, for the JKR contact, due to adhesion forces, this does not hold. The value of the non-zero pull-off force represents the adhesion of the contacting sphere with the flat. Strictly speaking, this force corresponds to adherence of the surfaces as energy dissipation, surface relaxation, etc. also influence its value. It should be stressed, that the value of the JKR *pull-off force* only depends on the sphere (lens) radius and the work of adhesion (adherence) in the medium in which the JKR experiment is conducted. Thus the contact area and mechanical properties do not play a role for its value.[3]

All the above considerations for contact mechanics were based on pairwise additivity of molecular forces. The role of the medium in which contacting and pull-off is performed, has not been discussed so far. However, the surroundings obviously influence surface forces e.g. via effective polarizability effects (essentially multi $\nu > 0$-body interactions e.g. by the presence of a third atom and its influence via instantaneous polarizability effects). These

[3] Several other contact mechanics theories have been put forward, which are not described in detail in this contribution. The most important ones of these theories for AFM applications include the Derjaguin-Muller-Toporov (DMT), the Burnham-Colton-Pollock (BCP) and the Maguis mechanics, see in 15,16. These theories differ in the assumptions (and limitations) and yield different expressions for the pull-off force. For example, the DMT theory, which assumes that long-range surface forces act only outside the contact area (as opposed to JKR, where adhesion forces only inside the contact area are assumed), predicts a pull-off force of 2πRW; compare with the JKR expression of Eq. 30.

effects can become noticeable in condensed media (liquids) when the pairwise additivity of forces can essentially break down. One solution to this problem is given by the quantum field theory of Lifshitz [120], which has been simplified by Israelachvili [113]. The interaction is expressed by the (frequency-dependent) dielectric constants and refractive indices of the contacting macroscopic bodies (labeled by 1 and 2) and the medium (labeled by 3). The value of the Hamaker constant A_{total} is considered as the sum of a term at zero frequency ($\nu = 0$, dipole-dipole and dipole-induced dipole forces) and London dispersion forces (at positive frequencies, $\nu > 0$).

$$A_{\text{total}} = A_{\nu=0} + A_{\nu>0} \approx \frac{3}{4} kT \left(\frac{\varepsilon_1 - \varepsilon_3}{\varepsilon_1 + \varepsilon_3}\right)\left(\frac{\varepsilon_2 - \varepsilon_3}{\varepsilon_2 + \varepsilon_3}\right) + \frac{3h\nu_e}{8\sqrt{2}} \frac{\left(n_1^2 - n_3^2\right)\left(n_2^2 - n_3^2\right)}{\left(n_1^2 + n_3^2\right)^{0.5}\left(n_2^2 + n_3^2\right)^{0.5}\left[\left(n_1^2 + n_3^2\right)^{0.5} + \left(n_2^2 + n_3^2\right)^{0.5}\right]} \quad (31)$$

Here ν_e is the main electronic absorption frequency in the UV, typically around $3 \times 10^{15}\ s^{-1}$ [113]. An analysis of the above equation shows some interesting consequences. A close match between the dielectric constants of the interacting bodies leads to diminishing values of the first term. The second term (determined by the refractive index values) shall then play the dominant role in the surface forces in this case. This effect can be utilized in "force spectroscopy" to maximize pull-off forces. On the other hand, interaction forces can also be minimized by a proper choice of the medium. Both these aspects will be important later for AFM-based force spectroscopy.

5 Atomic Force Microscopy with Chemically Functionalized Tips ("Chemical Force Microscopy", CFM)

As mentioned in the introduction, chemical force microscopy (CFM)[4] is an AFM-based technique, which allows one to determine and map the distribution of chemically distinct functional groups. Owing to the small tip-sample contact area, this mapping can be performed down to the sub-50 nm level [17]. The technique is based on the controlled chemical modification/functionalization of AFM probe tips in order to control the interaction between tip and the sample surface. Depending on the exposed functional groups and the medium, attractive or repulsive van der Waals forces, forces between dipoles, H-bonding, and electrostatic repulsion, among other forces,

[4] Chemical force microscopy (CFM) is used as a synonym for "AFM using defined surface chemistry, for instance self-assembled monolayer functionalization, on AFM probe tips in order to measure differences in surface chemical composition" (using friction or adhesion differences related to interactions between functional groups or atoms exposed on both tip and sample surface as contrast) throughout this review article.

may occur (see Sect. 4). The chemical contrast necessary for "imaging" is achieved by exploiting the spatial or temporal variations of these forces in quantitative measurements of the pull-off and/or friction forces between the tip and selected areas on the surface of interest. This approach is in particular promising for high resolution studies of functional group distributions in surface-treated polymers [57, 58, 110, 121–138].

5.1 The Case of Chemically Sensitive Imaging of Surfaces by Atomic Force Microscopy

5.1.1 Atomic Force Microscopy

Atomic force microscopy has developed into a mature technique for quantitative topography imaging of solid materials, including polymers. In the basic mode, called contact mode AFM, a very sharp probe tip, which is attached to a cantilever (typical spring constant of 1.0–0.1 N/m), is scanned across the sample surface (Fig. 7). The accurate positioning of the tip or, as shown in Fig. 7, the sample under a stationary tip, is achieved by piezo actuators. While the tip is scanned over the sample surface, the deflection of the cantilever is measured using a position-sensitive photodiode. A feedback loop holds a preset cantilever deflection constant by adjusting the piezo extension ("constant force mode"). A graphic representation of the adjustment of the piezo actuator's vertical extension as a function of lateral position yields the sample

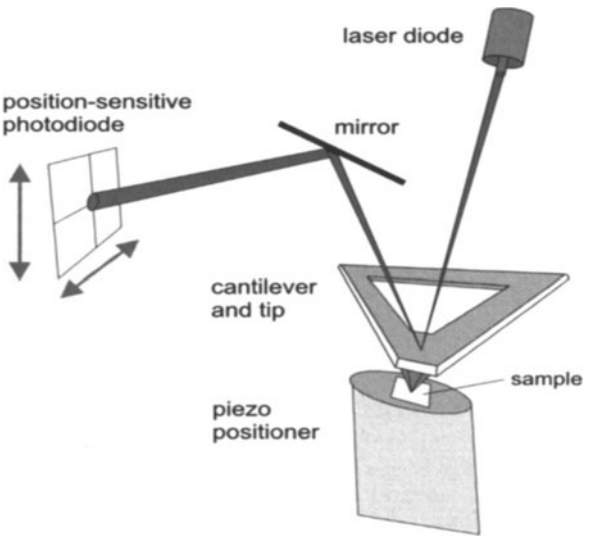

Fig. 7 Schematic diagram of contact mode AFM. (Adapted with permission from [143])

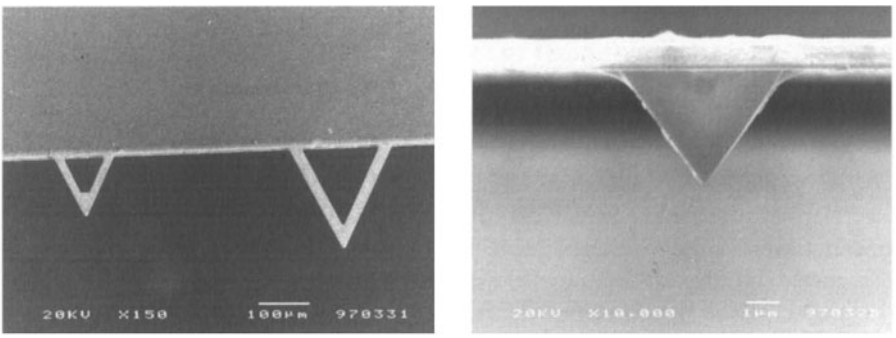

Fig. 8 SEM image of contact mode AFM cantilevers (*left*) and tip (*right*) (Reprinted with permission from [143])

topography (surface profile). The deflection of the cantilever is a result of the (repulsive and attractive) interactions between the atoms of the tip and the atoms of the sample surface, hence the name *force* microscopy. The nature of the various tip - sample interactions and their dependence on the tip - sample distance have been discussed in the literature [113, 116].

AFM tips, which are often made of silicon or silicon nitride, possess a radius of curvature at the apex between ca. 10 and (several) 100 nm nanometers. SEM images of two typical cantilevers and a tip are shown in Fig. 8. The tip radius, which ultimately limits the true lateral resolution [139], can also be determined based on high resolution SEM images or calibration gauges such as $SrTiO_3$ crystals [140]. AFM experiments are often performed in ambient conditions, however under these conditions a contamination layer (including water) gives rise to sometimes significant capillary forces [141]. AFM experiments can also be performed in other gases, in liquids, or in (high) vacuum. By performing measurements in liquids utilizing a liquid cell, the problem of capillary forces can be conveniently eliminated [142].

5.1.2 AFM-Based Force Measurements

Chemically sensitive imaging can be achieved in a general sense if a particular mode of AFM is sensitive to differences in a materials properties, which are then related to certain chemical functionalities exposed at or near the surface.

Differences in, for instance, modulus can give rise to excellent materials contrast in force modulation mode AFM or intermittent contact mode AFM phase imaging [144–146]. However, since this imaging contrast is not directly related to exposed functional groups and rather depends only on mechanical properties (including different indentation depths or energy dissipation), these and related approaches will not be considered here as chemically sensitive imaging [2, 147].

By contrast, normal forces and in some case lateral (friction) forces between the AFM probe tip and the sample surface are intimately related to exposed functional groups and will hence be treated in detail. CFM utilizes predictable and often specific interactions between functional groups in order to detect and identify functional groups with sub-100 nm resolution (see Sect. 5.1.3). The central idea of CFM is to control the interaction between tip and sample surface by chemically modifying the tip (Scheme 1). The interaction between such chemically modified tips and well-defined model surfaces composed of monolayers on gold, which expose different functional groups at the surface, was shown to depend on the nature of the interacting functional groups. These observations were consistently made in both pull-off force and friction measurements [17].

Pull-off force experiments and friction mode AFM with unmodified tips can be utilized to measure differences on chemically heterogeneous surfaces and have been shown to differentiate between chemically distinct phases in phase separated LB films, etc. However, the tip functionality cannot be varied and therefore, this approach is inherently limited [148].

In a standard contact mode AFM set up both repulsive and attractive forces between sample and surface can be measured with a high accuracy (force-displacement curves, force-distance curves, force spectroscopy). Examples include electrostatic forces, electrostatic double layer forces, hydrogen bonding, van der Waals interactions, and magnetic forces. The resolution limit for an optical detection system and typical commercial spring constants has been estimated to be in the order of 10^{-11} N [149]. Depending on the detection system, the force constant, the stiffness, and the resonance frequency of the cantilever even smaller forces are in principle measurable using designer cantilever-tip assemblies [150, 151].

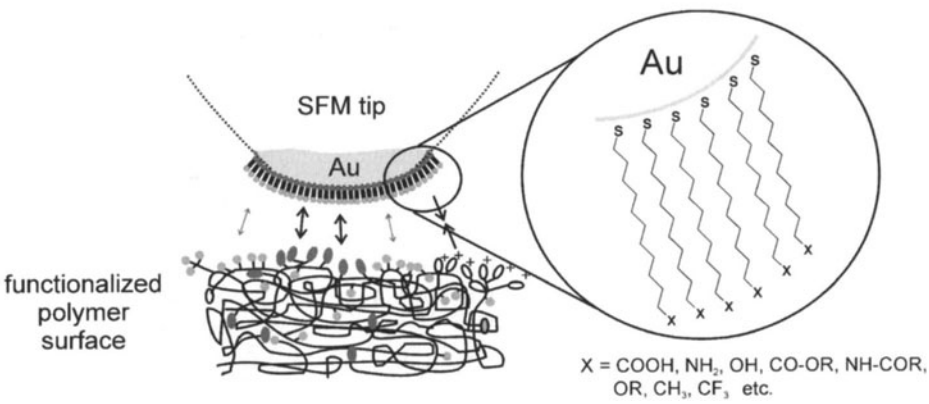

Scheme 1 Schematic drawing of monolayer-modified SFM tip used for CFM and interactions between exposed functional groups on the contacting surfaces (Adapted with permission from [143])

In a standard force displacement experiment the sample is moved up and down (in and out of contact with the tip) at a fixed position (x, y) [15, 152]. In Fig. 9, the corresponding movements of piezo (sample) and cantilever deflection, and the resulting force displacement curve are schematically depicted. The adhesion is characterized by the so-called pull-off or pull-out force (sudden jump of force when the tip breaks free from the surface). This force is related via the corresponding surface free energies to the functional groups exposed on the contacting surfaces and also the medium in which the experiment takes place (see below). A quantitative determination of forces requires a thorough calibration of the cantilever spring constant [15, 152–155].

A second viable option to perform chemically sensitive AFM imaging in a general sense is using the lateral force, or friction mode. This is based on the "semi-quantitative" relationship between adhesion (adherence, pull-off) and friction. In contact mode AFM, friction forces can be measured simultaneously with topography imaging in constant force mode. In order to maximize the sensitivity of friction force measurements the sample is scanned in an angle of 90° with respect to the long axis of the cantilever. The torsion of the cantilever around its long axis is measured with a 4-quadrant photodiode (for schematic see Fig. 7). A representative example for the corresponding output of the photodiode signal is shown in Fig. 10. The so-called friction loop displayed here allows one to calculate the friction force from the difference of the trace and retrace line multiplied by 0.5. In order to improve the statistics one typically acquires a complete scan simultaneously for both relative scan directions (trace and retrace) and calculates the mean friction forces from the corresponding difference image.

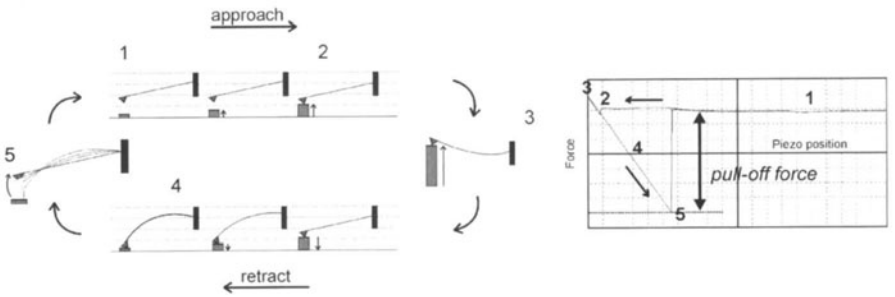

Fig. 9 Measurement of force distance curves (*left*); Schematic force-distance plot (*right*): The sample is approaching the tip (1, top); at some distance the gradient of the force overcomes the cantilever spring constant and the tip jumps into contact (2); further movement up causes a deflection of the cantilever (3); during retraction the tip "sticks" usually much longer to the surface (4) and snaps off when the spring constant overcomes the force gradient (5). The adhesion between tip and sample is characterized by the so-called pull-off or pull-out [156] force (snap off). (Adapted with permission from [143])

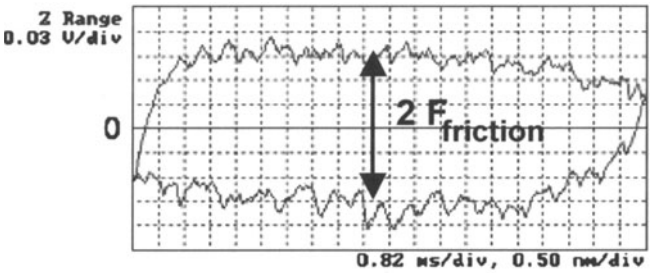

Fig. 10 Friction loop (friction force vs. scanned distance plot) measured perpendicular to the polymer chain direction of oriented polyethylene with a $-CF_3$ modified tip [131]. The photodiode output signal in Volts is directly proportional to the friction force (Reprinted with permission from [143])

Quantitative measurements of friction forces are complicated by the geometry in the case of triangular shaped cantilevers, variations of photodiode sensitivity, the dependence of the photodiode output signal on laser alignment and the difficulty of accurate calibration of the lateral force spring constant [157]. Furthermore, since the friction forces are related to energy dissipation, these forces may depend on factors other than the chemical nature and variation of the functional groups exposed. Examples include polymer specimens with orientational order on various length scales (molecular, lamellar) or monolayer systems, which possess differences in conformational order (see below).

In order to utilize pull-off forces obtained in force-displacement measurements, or friction forces in lateral force microscopy (LFM) measurements for chemically sensitive imaging, the relation of these forces and chemical functionality must be established. For pull-off forces, (continuum) contact mechanic theories, including the JKR theory, have yielded a satisfactory description of the experimental data [119]. For the idealized geometry of a sphere with radius R interacting with a flat planar surface, the JKR theory predicts that the contact area is a function of R, the moduli of the sphere and surface material (through the reduced modulus K, see Eq. 27), the surface energy per unit area W_{123} (Eq. 17) and load L (compare Eq. 28). The pull-off force thus derived (Eq. 30) depends only on the sphere radius and the surface energy per unit area/work of adhesion W_{12}, which may be expressed as a function of the surface free energies of the tip (γ_1), the sample γ_2, and the corresponding interfacial free energy γ_{12} (Eq. 32). If the experiment is carried out in a medium, the γ_i refer to the surface free energy for the surface i in contact with the corresponding medium.

$$W_{12} = \gamma_1 + \gamma_2 - \gamma_{12} \tag{32}$$

As mentioned, the central idea behind CFM is to exploit differences in long and short range forces via (a) the control of the tip chemical composition by assembly of a functionalized monolayer (see below), thus via control of the

surface free energy of the tip, and (b) via control of the medium.[5] By correlating the forces obtained in force-displacement measurements with surface energies based on these equations it is possible to discriminate between different materials and specimens of a given material with different surface energies. This approach can be combined with spatially resolved adhesion force imaging by sequential pull-off force data acquisition. As an example for spatially resolved adhesion data we show in Fig. 11 the spatially resolved friction and force data measured on a solution-grown polyethylene (PE) lamella deposited on mica. The interaction between the Si_3N_4 tip and the hydrophobic PE crystal is weaker than the interaction between the tip and the underlying mica substrate. As this data were acquired in air, the contribution of capillary forces must be considered as well. Typically, CFM measurements are carried out in a liquid environment to eliminate these forces. The friction contrast in the lateral force mode image shown on the left, however, is dominated by the difference in friction force due to the different orientation of folds in different fold sectors.

The localization of different functional groups exposed at various polymer surfaces is more challenging. For chemically complex polymer surfaces, such as surface-treated polymers, the variation in chemical nature of the func-

[5] For a discussion of manipulation of the sum of van der Waals forces via an appropriate choice of solvent, see [125].

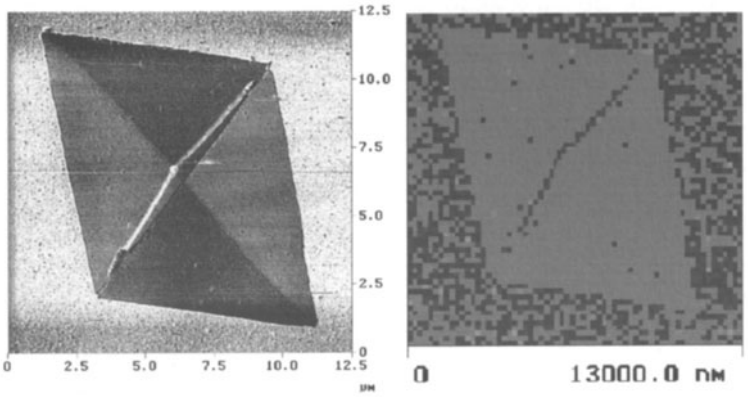

Fig. 11 Friction force micrograph of PE lamella on mica (*left*, friction forces increase from dark to bright contrast) and laterally resolved adhesion forces (*right*, dark: – 80 nN, bright: – 50 nN pull-off force) collected in the so-called force-volume (FV) mode (see Sect. 5.2.2). Since the measurement was carried out in air, the forces are dominated by capillary forces. The contrast in the friction force micrograph is related to the orientation of the folds on the polymer lamella surface, which are oriented along the crystal edge in each sector. (Reprinted with permission from [158]. Copyright 1999 American Chemical Society)

tional groups exposed will result in many different interactions with the tip (Scheme 1). If these different interactions can be understood, the detection of chemically distinct species with high spatial resolution becomes feasible. The spatial resolution is limited by the range of the operating forces or by the sharpness of the probe tip. In a first approximation we can state the contact area at pull-off A_0 according to the JKR theory. For typical values we obtain an area of < 10–100 nm^2, i.e. < 50–500 molecules of a monolayer (see below).

$$A_0 = \pi \left(\frac{3\pi R^2 W_{12}}{2K} \right)^{\frac{2}{3}} \tag{33}$$

5.1.3
AFM Probe Functionalization, Surface Imaging and Surface Chemistry

The standard AFM tip materials silicon (rather SiOx) and silicon nitride, as well as various metal and oxide coatings applied by evaporation or sputtering, can be used in conjunction with different liquid environments to vary the interaction between tip and surface in a controlled way. While these tip functionalities may be useful in CFM experiments, a much richer variety of tip functionalities is in many cases required, to allow for instance for (specific) hydrogen-bonding, hydrophobic or hydrophilic interactions. Thus, the need to control and deliberately vary the surface free energy of the tip (e.g. γ_1) can be met by procedures for controlled tip functionalization. Among the requirements for tip functionalization procedures are ease and reliability of preparation, chemical and mechanical robustness of the deposited layers, and a wide variety of functionality (different functional groups). These requirements are met by using self-assembled monolayers (SAMs). These are monomolecular layers, which are formed by spontaneous adsorption and organization at the solid-liquid or solid-gas interface. These layers are highly ordered, thus the alkane chains possess conformational order, the end groups that dominate the corresponding surface energy are exposed at the layer surfaces, and the anchoring headgroups are bound to the tip. The most popular procedures will be briefly explained.

The free hydroxyl groups exposed on standard AFM tip materials SiOx and silicon nitride can be directly functionalized using chloro- or ethoxy-substituted alkanesilane chemistry (Fig. 12 left). When proper reaction conditions are used, SAMs can be deposited onto the tip. These procedures are complicated by crosslinking reactions for the typically used trichloro- or triethoxysilanes, by variations in the number of silanol groups exposed on the tip surface, and details of the derivatization procedure.

A severe limitation is related to the limited number of functional groups, which can be introduced in the ω-position of the alkane substituent due to unwanted side reactions. An alternative approach relies on the forma-

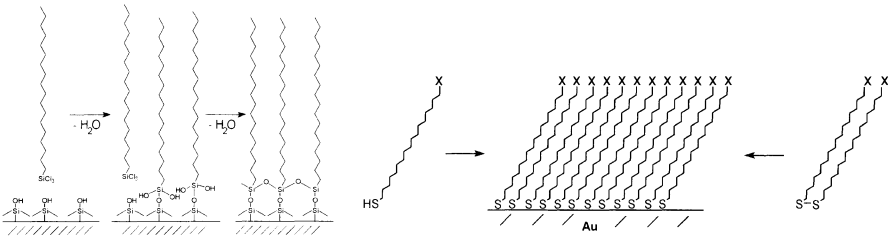

Fig. 12 *Left*: Schematic drawing of the idealized condensation reaction of trichlorosilanes on oxidized silicon, which leads to an internally cross linked SAM. *Right*: Schematic drawing of self-assembly of n-alkanethiols and disulfides on gold. Thiol and disulfide molecules which are functionalized in the ω-position, can be utilized leading to functionalized SAMs. (Reprinted with permission from [143])

tion of SAMs on noble metals, such as gold. AFM tips can be coated by a thin layer of Au (one to few nm of Cr or Ti is used as an adhesion promoting layer between Au and the tip), which is then simply immersed into a solution of a ω-functionalized alkanethiol or disulfide. After several hours of assembly the tip can be rinsed and dried, and is reliably functionalized. Many functional groups are compatible with this chemistry, thus $-CH_3$, $-CF_3$, $-CO-OCH_3$, $-CH_2-OCH_3$, $-CO-NH_2$, $-NH_2$, $-OH$, $-COOH$ and many other groups can be incorporated. The caveat of this procedure is the increase in mean tip size. The evaporated Au layers are granular (Fig. 13).

The SAMs used for tip modification, being versatile in terms of surface chemistry (exposed functional groups), homogenous, and practically defect-free, are ideal model systems for interfacial studies and thus served as model systems for the first CFM studies. In the histograms shown in Fig. 14 the differences in pull-off force between a $-COOH$ functionalized tip and two different pairs of surfaces is summarized. The mean pull-off forces calcu-

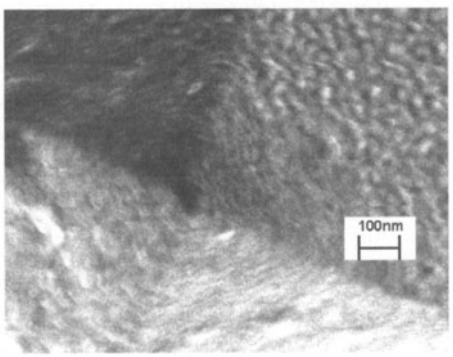

Fig. 13 High resolution SEM image of a gold/SAM coated AFM tip. (Reprinted with permission from [143])

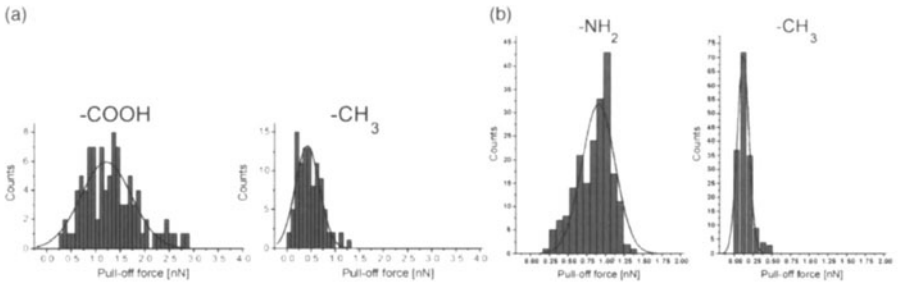

Fig. 14 (**a**) Histograms of pull-off forces measured with a – COOH tip on – COOH (*left*) and – CH_3 terminated SAMs (*right*) in ethanol (*curves*: Gaussian fits). The average pull-off forces are 1.21 ± 0.51 nN (– COOH) and 0.42 ± 0.25 nN (– CH_3); (**b**) Histograms of pull-off forces measured with a – COOH tip on – NH_2 (*left*) and – CH_3 terminated SAMs (*right*) in ethanol (*curves*: Gaussian fits). The average pull-off forces are 0.90 ± 0.22 nN (– NH_2) and 0.12 ± 0.08 nN (– CH_3) (Reprinted with permission from [57]. Copyright 2000 American Chemical Society)

lated from the histograms show that carboxyl groups and methyl groups, and amino groups and methyl groups, respectively, can be differentiated in force measurements in ethanol.

From the force histograms it is evident that areas in monolayer systems, which expose different chemically distinct functional groups, can be differentiated in pull-off force measurements. In Fig. 15, the first example of CFM force imaging published by the Lieber group is shown [17]. Here a patterned SAM exposing – CH_3 and – COOH groups was imaged (friction contrast) with a – CH_3 and a – COOH terminated tip in ethanol. The friction contrast shows in accordance with adhesion measurements that the interaction between carboxylic acid groups in ethanol is stronger than the mixed interaction between methyl and carboxyl groups.

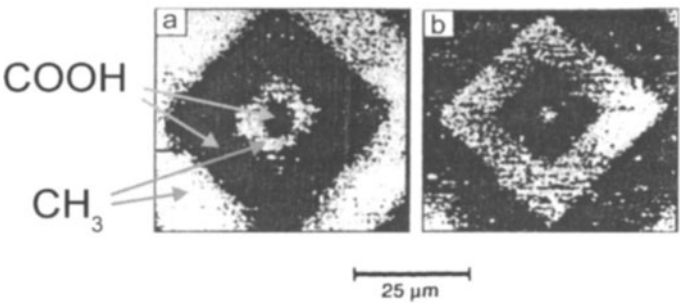

Fig. 15 Friction force image recorded on a patterned – CH_3/– COOH monolayer sample with (**a**) a – CH_3-terminated tip and (**b**) a – COOH-terminated tip in ethanol. The friction forces, which increase from dark to bright contrast, show a contrast reversal. (Adapted/reprinted with permission from [17]. Copyright 1994 AAAS)

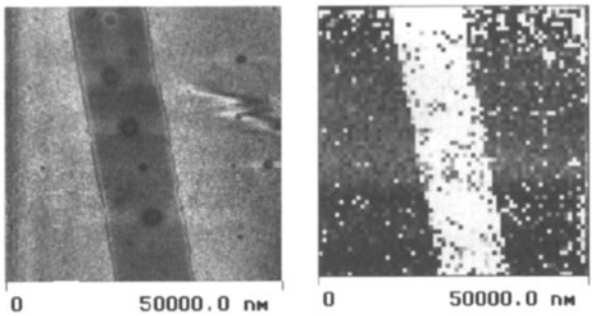

Fig. 16 AFM friction force micrograph (*left*, $z = 0.2$ V) and FV (see Sect. 5.2.2) force image (*right*, $z = -20$ nN) measured with a $-CH_3$ modified tip on patterned SAM exposing a hydrophilic $-OH$ stripe in a hydrophobic cholesterol-terminated matrix in water. In the FV image darker color corresponds to higher pull-off forces. (Reprinted with permission from [163]. Copyright 1999 American Chemical Society)

Rapidly after the first report, a number of groups have reproduced the original contact mode results and complemented the observations and the results of the Lieber group [57, 58, 110, 125–132, 134, 135, 137, 138]. One of the spectacular results is the chiral recognition reported by McKendry et al. [134] A very closely related field is the so-called single molecule force spectroscopy [121, 159, 160]. Here AFM tips are functionalized e.g. with ligand molecules. Specific interactions with surface-immobilized receptors are measured. Examples include exclusively relatively large molecules, often with biological relevance, such as DNA, cell adhesion molecules, or streptavidin [121, 159]. This method can also be extended to measure individual supramolecular host-guest interactions of small molecules, which possess fast unbinding kinetics [121, 161, 162].

A second example for CFM imaging is shown in Fig. 16. Here a hydrophobic $-CH_3$ terminated tip is used to differentiate between hydrophilic and hydrophobic regions in a microcontact printed SAM in friction and adhesion (pull-off) force measurements in water [163].

In addition to chemically sensitive imaging, the control of tip-sample interactions by means of tip functionalization has been exploited by various authors to improve the imaging forces and thus force contrast [164–166].

We can summarize at this point that the forces measured in AFM adherence force (and frequently friction) measurements depend crucially on the chemistry of the AFM tip and the surface of interest, as well as the medium in which the contact takes place. Hence by systematic variation of the tip chemistry via chemical modification/functionalization and of the medium chemical contrast spatially resolved chemical imaging becomes possible.

5.2 CFM on Polymers – Friction and Pull-Off Force Imaging/Mapping

Reports on CFM-based imaging by force mapping of well-defined model surfaces, mainly composed of SAMs, are abundant in the literature. By contrast, there are much fewer reports on the application of CFM imaging on polymers. Expanding on the basic features of the friction force and pull-off force data acquisition, the simplified interpretation based on continuum contact mechanics, and the discussion of various examples of CFM data based on force-displacement (f-d) curves and pull-off forces discussed above, we will shift our focus here to the spatially resolved acquisition of force and friction data on polymers. Since the "tip functionality" of any tip material can very well be defined and may offer the basic requirement of CFM regarding chemical contrast, we will also treat some results obtained with "unmodified" tips.

5.2.1 Friction Force Imaging

CFM friction imaging using modified AFM tips is, as far as the imaging technique and data acquisition are concerned, the same as conventional friction force or lateral force imaging in contact mode AFM. In order to maximize sensitivity, the relative scanning direction of the tip with respect to the sample is carried out such that the scanning direction is perpendicular to the long axis of the cantilever (compare Fig. 7). The image contrast, correctly derived from a difference image of retrace subtracted from trace divided by 2, can be predicted in the case that adhesive interactions are dominant. The magnitude of the friction force is proportional to the contact area A, which can be calculated as a function of work of adhesion following e.g. Equation 28. Based on this equation, a local increase in work of adhesion leads to an increase in magnitude of the measured friction force.

One early example described by Sinniah et al. [138] shows that AFM tips functionalized with various alkanethiols can be utilized to differentiate polyamide-rich regions from poly(ethylene glycol)-rich regions in a blocky segmented copolymer in water (Fig. 17). In this particular case, the friction forces observed with the more hydrophobic methoxy-terminated tips on the polyamide-rich domains exceed the forces measured on the PEG-rich domains. Using amide-terminated tips, the contrast is significantly reduced, which implies imaging with predictable contrast.

A similarly clear and predictable contrast has been reported by Feldman et al. for a phase separated blend of polystyrene (PS) and poly(methyl methacrylate) (PMMA) imaged with gold-coated and silicon oxide coated tips in perfluorodecalin (Fig. 18) [125]. Here the contrast is dominated by the dispersive van der Waals interactions, which have been selectively amplified by

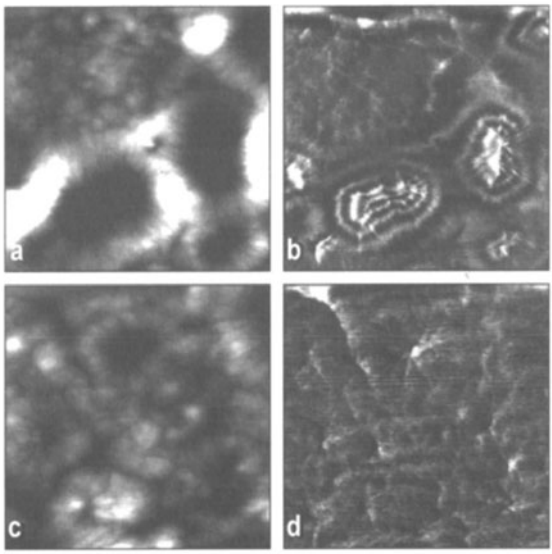

Fig. 17 Solvent-exclusion contribution to image contrast is demonstrated with scanning force data acquired on a co-block-polyethylene glycolpolyamide (Nylon-12) surface (PEBAX 1074), prepared by melting/resolidification. (**a**) Topographic image in water, methoxy tip termination (15 μm × 15 μm); (**b**) friction image in water, methoxy tip termination (15 μm × 15 μm); (**c**) topographic image in water, amide tip termination (7.5 μm × 7.5 μm); (**d**) friction image in water, amide tip termination (7.5 μm × 7.5 μm). (Reprinted with permission from [138]. Copyright 1996 American Chemical Society)

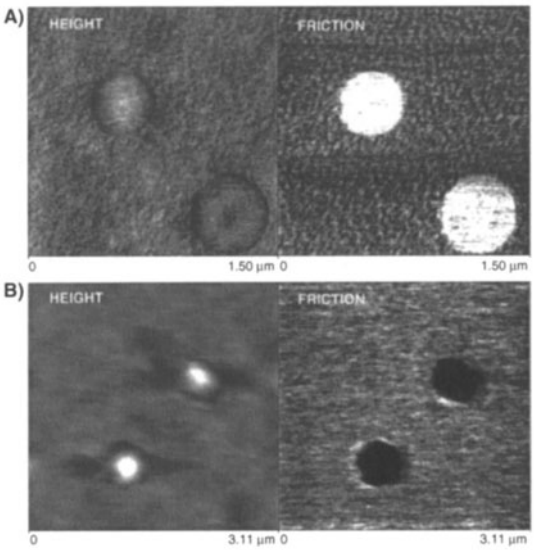

Fig. 18 Height (AFM) and friction (LFM) images of a spin-cast polystyrene/poly(methyl methacrylate) polymer blend [PS/PMMA (1 : 10 w/w)], obtained with (**a**) gold-coated and (**b**) SiO_x tips under perfluorodecalin. (Reprinted with permission from [125]. Copyright 1998 American Chemical Society)

a clever choice of the solvent as discussed above. The gold-coated tip experiences higher friction forces on the PS compared to PMMA, while the silicon oxide terminated tip shows an inverted contrast. This example shows how the Lifshitz theory earlier mentioned can be successfully applied to predict the chemical contrast for various apolar polymers imaged by different tips in cases where the optical constants of the materials in question are known or can be determined. The chemical contrast on (more) polar surfaces, including polymers that have undergone an oxidative surface modification, cannot be predicted in a similar way (see below).

The resolution of friction imaging is limited by the effective tip-sample contact area and thus by the sharpness of the chemically modified probe (the contact area in principle varies with the variation of surface composition due to changes in the JKR forces). This sharpness can be described by a tip radius of 10–100 nm, depending on the procedure used. Werts et al. have reported on successful CFM imaging of a microphase-separated block copolymer (PS-PVP hetero-arm star copolymer), which implies a lateral resolution of better than ~ 30 nm [167]. On thin microtomed sections of microphase-separated polymer films the friction contrast measured in an argon atmosphere was pronounced with a carboxylic acid-functionalized tip, as shown in Fig. 19, while methyl-terminated tips yielded no contrast between the microphase separated domains. This observation was interpreted by the authors as chemical contrast, i.e. polystyrene and poly(2-vinylpyridine) can be differentiated owing to the strong interactions between the carboxylic acid groups on the tip and the pendant pyridine groups of the 2-PVP block.

The clear advantage of friction imaging compared to pull-off force mapping is the ease of the experiment and the relatively rapid data acquisition. Scan velocities of several micrometers per second are feasible, hence typical images can be recorded within one to a few minutes and possible instru-

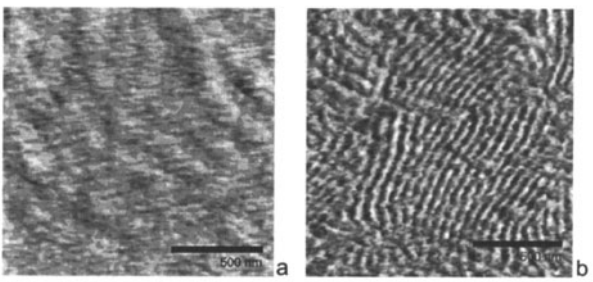

Fig. 19 Friction force images (1.5 μm × 1.5 μm) obtained by means of CFM (**a**) with a $-CH_3$ tip and (**b**) with a –COOH tip. Since the friction coefficients determined with a $-CH_3$tip are nearly the same on PS as PVP, the lamellar structure is not visible in (**a**). With a –COOH tip the friction coefficient is higher for the PVP part of the copolymer, which reveals the morphology as the alternating bright (high friction, PVP) and dark (low friction, PS) areas. (Reprinted with permission from [167]. Copyright 1998 Wiley-VCH)

mental drift in liquid media can be tolerated to a certain extent. Possible disadvantages include an increased tip-sample contact area (compared to the situation at pull-off in a f-d experiment, see Eqs. 33 and 28) and a contact area variation at a constant load due to variations of the JKR forces. Hence lower lateral resolution, and the possibility of tip or sample damage as a result of significant shear forces may arise. The interpretation of experimental data is sometimes complicated by friction forces, which are not dominated by adhesive interactions. Alignment on the molecular scale (polymer chains in crystalline areas [131, 168, 169] or at the fold surface of solution-grown lamellar crystals, see also Fig. 11 left) [158, 170–172] may lead to pronounced friction anisotropy; we have for instance measured differences in friction signal of a factor of > 4 depending on the orientation of PTFE chains with respect to the stationary scanning direction of the tip [169, 170]. Further, variations in modulus (Eq. 28) may dominate over the work of adhesion and render interpretation of the image contrast difficult without additional experimental data or independent knowledge. The most serious limitation is the intrinsic difficulty to perform truly quantitative friction imaging, which is required to obtain values of surface free energy similar to the data extracted from f-d curve measurements. Besides the calibration of the lateral spring constant of the cantilever, the calibration of the photodiode (sensitivity) is a major challenge [157]. The best option is obviously to analyze friction force data and subsequently captured pull-off force data (for an example see below).

5.2.2 Pull-Off Force Imaging

The alternative imaging mode for laterally visualizing chemical or compositional differences in CFM involves spatially resolved f-d curve data acquisition. As briefly mentioned above, several approaches as to how to tackle this experimental challenge have been proposed [173–178]. The basic approach is to record f-d curves for each pixel of a mesh of pixels. A simple method is the display of the data as a so-called force volume (FV) image. In this approach the deflection data are sliced and sorted in deflection values that are larger and smaller than some arbitrarily chosen value. Since this mode displays the deflection values with respect to a reference point and not true pull-off forces, care must be taken when such data are interpreted. For instance, f-d curves displaying a large hysteresis may show a strongly negative (deflection = force) value in the force volume image, which may erroneously imply large pull-off forces. The best way to analyze and display the data is by an automated software procedure in which each force-displacement curve recorded for each single pixel is analyzed off-line. The corresponding data, e.g. magnitude of the pull-off force, can be displayed on a 2-D map of forces (adhesion map) or can be treated statistically to yield a mean value of the pull-off force. In

the latter case an image with a limited number of pixels, e.g. 64×64 points^2, yields a mean of 4096 force-distance measurements [179].

A comparison with subsequently recorded height images can be useful to exclude some well-known artifacts. The interpretation of force data on the basis of the continuum contact mechanics (e.g. JKR theory, see Sect. 4.2) relies on the idealized situation of a spherical tip interacting with a flat surface; however, in practice, surfaces are in most cases "rough" [132, 133]. Protrusions on the sample surface lead to a local variation in tip-sample contact area. Depending on the geometry near the area of contact, i.e. non-conformal tip-sample contact or contact between tip side-wall and a protrusion, this may lead to an underestimate, or an overestimate, respectively, of the "true" pull-off forces [132]. Two illustrative examples are shown in Figs. 20 and 21.

In Fig. 20, a height and a corresponding force volume image are shown, which were recorded with a $-CH_3$ terminated tip on an octadecanethiol SAM on a granular gold surface. In force-volume images the pull-off forces can be graphically displayed in a layered image. Pull-off forces larger than a certain value are displayed in a gray scale. As an attractive force has per definition a negative sign, the scaling ranges from dark tones (high pull-off force) to bright tones (low pull-off force). The influence of the tip-sample contact area is clearly seen. The pull-off forces are smallest on top of the grains, where the contact area is minimized, while the highest forces are measured between the grains. The differences in contact area on this chemically absolutely homogeneous, but granular, surface (rms roughness on this image scale 3–5 nm) can already give rise to artifacts in CFM.

Artifacts due to contact area variations can also be observed, when features with sizes of several hundred nanometers are imaged. In order to illustrate this problem, poly(vinyl alcohol) (PVA) fibers, prepared by elec-

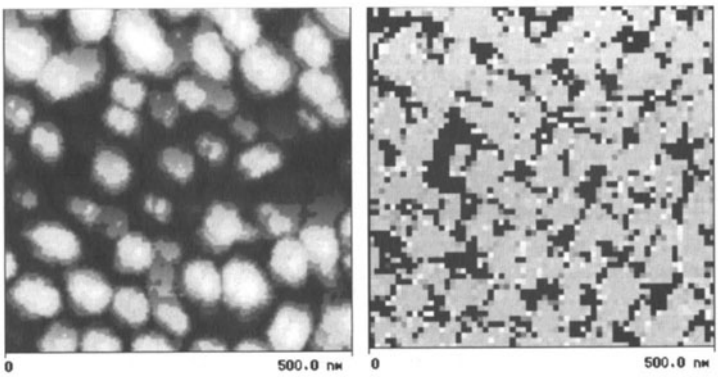

Fig. 20 Height (*left*) and FV images (*right*) of octadecanethiol SAM on granular gold surface obtained with $-CH_3$ terminated tip in air. The gray scale denotes: bright (low forces) to dark (high forces), -5 nN to -21 nN. (Reprinted with permission from [143])

trospinning [180, 181], were imaged on SAMs using functionalized tips. The pull-off force differences between the polymer and the substrates varied systematically when fibers with a diameter of one or several micrometer were imaged [143]. For thinner fibers the pull-off force images revealed a clear inhomogeneous pull-off force on the polymer fiber itself (Fig. 21).

The occurrence of areas of high and low adhesive forces, which are oriented parallel to the PVA fiber axis, can be attributed to an increased and decreased effective contact area between the side of the tip as compared to the tip apex. As the fiber shape is not a priory known, no definite conclusions about the chemical contrast can be obtained. However, a careful comparison of topography and force data clearly reveals the artifact. These observations demonstrate that force maps, and force data in general, must be interpreted carefully. In particular, attention must be paid to avoid coupling of the topography into the force images.

The first example for the study of polymer surfaces by "adhesion force" mapping known to us is the report by Mizes et al., who studied polycarbonate with a conventional Si_3N_4 tip [173]. On the polycarbonate film depicted in Fig. 22, a clear contrast in the adhesion image is seen.

All methods based on the capture of individual force-distance, f-d, curves are conceptually similar to this first reported method. The acquisition of f-d data in a pixel-per-pixel fashion is intrinsically slow compared to friction imaging since the tip must be lifted out of contact for each pixel. In liquids the corresponding viscous drag forces limit data acquisition to rates of typically few pixels per second, thus, an image of 64 pixels × 64 pixels takes on the order of 8–12 min. For high resolution work, thermal and instrumental drift may therefore become serious problems. However, these drawbacks are often overcome by a much more straightforward data inter-

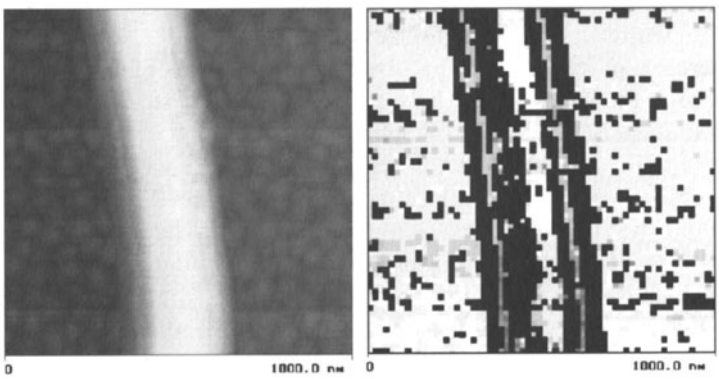

Fig. 21 Height (*left*) and FV force images (*right*) of electrospun fiber of PVA on SAM of octadecanethiol. The gray scale denotes: bright (low forces) to dark (high forces), – 4 nN to – 30 nN. (Reprinted with permission from [143])

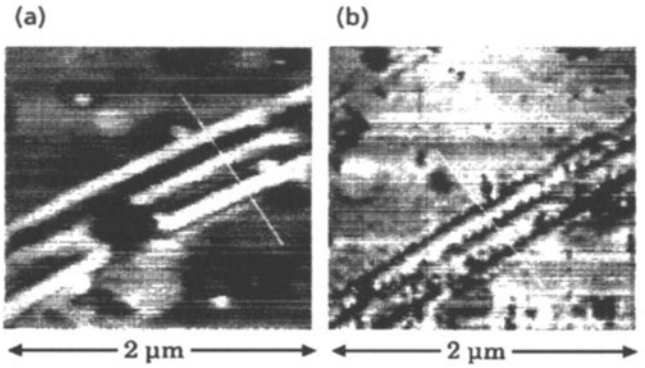

Fig. 22 (**a**) Topography of an undoped polycarbonate film; (**b**) Spatial variation in adhesion over approximately the same area. The adhesion ranges from 7.6 to 36.3 nN. (Reprinted with permission from [173]. Copyright 1991 American Institute of Physics)

pretation (as discussed above the pull-off forces do not depend on modulus, but only on tip radius and work of adhesion) and a significantly less complicated calibration of the cantilever spring constants and photodiode sensitivities [15, 16, 153–155, 157].

An improved experiment has been proposed and commercialized by the group of Marti [182]. In the so-called "pulsed force" mode, the sample is modulated sinusoidally ($\sim$ 1 kHz) during a conventional contact mode AFM scan with an amplitude, which is just large enough to overcome the adhesive interactions. Hence the tip contacts, indents, and breaks free from the surface with a frequency of $\sim$ 1 kHz during scanning. Instead of digitally recording the complete f-d curve, only the four points are captured, the baseline, the maximum repulsive force, the maximum adhesion force and a point that can be used with the maximum repulsive force to define the slope in the loading regime, respectively (Fig. 23). CFM data using this technique have been reported by Fujihira et al. on SAMs [183].

As mentioned in the introduction, the application of CFM on surface-treated polymers promises to be particularly useful to determine the lateral distribution of surface functional groups in liquid environments on the nanometer scale. Owing to the complexity of the conventional functionalization procedures, the imaging of particular functional groups is, however, difficult and the data interpretation may become challenging. The presence of many different functional groups with widely varying contributions to the intermolecular interactions discussed above, limits the successful mapping to phase-separated blends or morphologies (see examples above) on the one hand, and to "addressable" functional groups, such as acidic or basic groups, on the other hand. For the latter functional groups, it is possible to change the chemical character of the group in situ in the liquid cell of the AFM simply by changing the pH. Thus, while all interactions of pH-independent functional

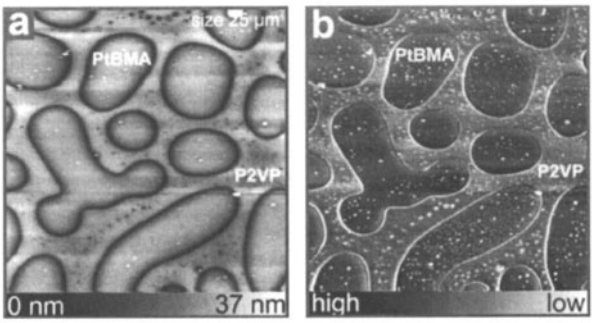

Fig. 23 Pulsed force mode measurement on two homopolymers spincoated on silicon from THF solution of a mixture of P2VP and PtBMA. The pulsed force mode AFM images clearly distinguish the PtBMA islands from the surrounding P2VP in both topography (**a**) and in adhesion (**b**). (Reprinted with permission from [184]. Copyright 2000 American Institute of Physics)

groups are unchanged or at worst predictably altered, the addressable groups change their behavior and become charged (or uncharged). This feature can be exploited in selective CFM imaging.

As an illustrative example we show below the surface of two modified (oxyfluorinated) isotactic polypropylene films [185] imaged in force-volume mode with a hydroxy-functionalized tip. The hydroxy end group of the alkanethiol used for tip modification shows pH-independent adhesive properties [124] and, owing to the low surface energy, the adhesion in aqueous medium is minimized on all surfaces. As shown in Figs. 24–26, the pull-off forces of various oxyfluorinated iPP films depend on the pH of the imaging solution (Fig. 24). This behavior is attributed to the deprotonation of the carboxylic acid groups introduced by the surface modification [57, 58, 110].

From an analysis of FV images of these specimens it becomes clear that the forces are heterogeneously distributed over the film surface at low and intermediate pH, while at high pH exclusively electrostatic repulsion is observed with no discernible pull-off force. A careful comparison with the additionally captured height images ensures that the observed differences in pull-off force are not due to differences in effective contact area. The areas in which attractive interactions are measured at pH 6.1 were interpreted to contain carboxylic acid groups with a higher "pK_a" compared to the regions where repulsion is observed. This observation was attributed to a difference in local hydrophobicity, in accordance with data reported by the Lieber group on SAMs [124]. The most hydrophobic local environments will be the areas where the deprotonation of carboxylic acid groups is least favored. Consequently, these areas will be more protonated at pH 6.1 compared to the more hydrophilic areas, thus areas with a high density of – COOH and – OH functionalities [58].

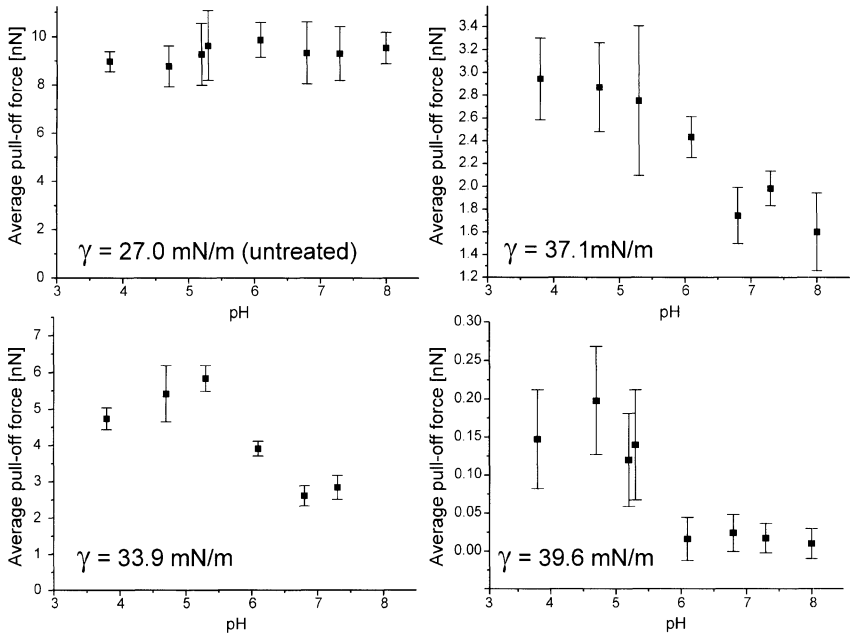

Fig. 24 Force titration of an untreated iPP (*top, left*) and three oxyfluorinated iPP films using OH-terminated SFM tips. The total surface tension values are indicated. The error bars correspond to the standard deviation of the average value calculated from the corresponding histograms. (Reprinted with permission from [58]. Copyright 2000 American Chemical Society)

A qualitatively similar observation was made on plasma polymerized allylamine films on oxidized Si (Fig. 27) [57, 121]. The force titration behavior was found to agree with the presence of primary amino groups that were identified independently by FT-IR spectroscopy and XPS. The shift in force pKa ($\sim$ 5.7) with respect to the solution pKa ($\sim$ 10.5) was attributed similarly to the above mentioned behavior of carboxylic acid groups to the effect of the hydrophobic environment; the more hydrophobic the local environment, the higher is the free energy of creating a charged amino group. The locally more hydrophobic environments will resist protonation stronger than hydrophilic areas and hence correspond to the areas of high pull-off force.

Another recent example of the use of CFM for polymer surfaces is force-volume mapping of stabilized polypropylene films (process stabilizers, UV-stabilizers and antioxidants) [186, 187]. The mapping was performed using methyl- or hydroxy- functionalized tips in water or in nitrogen atmosphere. Differences in the pull-off forces between the additives and polypropylene allowed imaging with sub-micrometer resolution of the lateral distribution of the additives present on the surface. By performing pull-off measurements on spin-coated films of pure additives, characteristic pull-off force values were obtained, which made it possible to discriminate between the antioxidant,

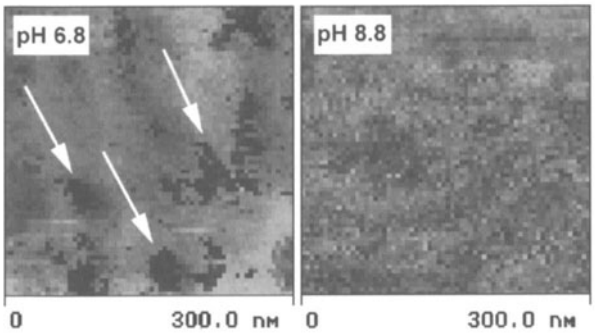

Fig. 25 FV images of oxyfluorinated iPP (γ = 39.6 mN/m) at pH 6.8 (*left*) and pH 8.8 (right). Dark color indicates high adhesion (– 0.3 nN for pH 6.8, $\approx$ 0 nN for pH 8.8), bright color indicates low adhesion (0 nN for pH 6.8 and pH 8.8). The arrows indicate areas of high pull-off forces, which were attributed to domains with the most hydrophobic character, i.e. lower density of polar – COOH and – OH functional groups introduced by the oxyfluorination). (Reprinted with permission from [58]. Copyright 2000 American Chemical Society)

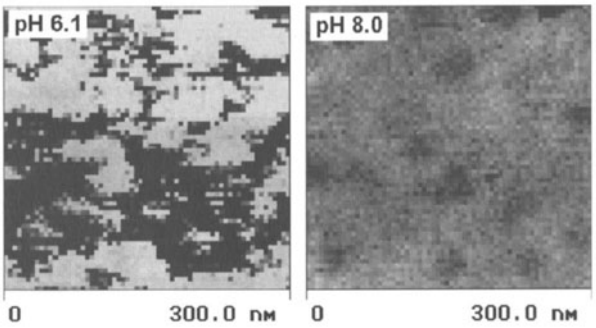

Fig. 26 FV images of oxyfluorinated iPP (γ = 37.1 mN/m) at different pH. In the force images dark color indicates high adhesion (– 1.3 nN, – 0.4 nN for pH 6.1 and pH 8.0, respectively), bright color indicates low adhesion (– 0.2 nN and $\approx$ 0 nN for pH 6.1, and pH 8.0, respectively). (Reprinted with permission from [58]. Copyright 2000 American Chemical Society)

which was more hydrophobic, and the UV-light stabilizers [187]. It was, however, pointed out that it was necessary to perform measurements using both tip modifications in both water and nitrogen atmosphere in order to identify an additive. Moreover, a gradual change of the average adhesion forces with aging time of the stabilized polypropylene films was correlated to a migration of additives from the bulk to the surface, gradually forming a film which made the surface less hydrophobic [186]. Time of flight (ToF) SIMS was used to confirm the presence of the additives, even though sub-micrometer resolution was not provided [187].

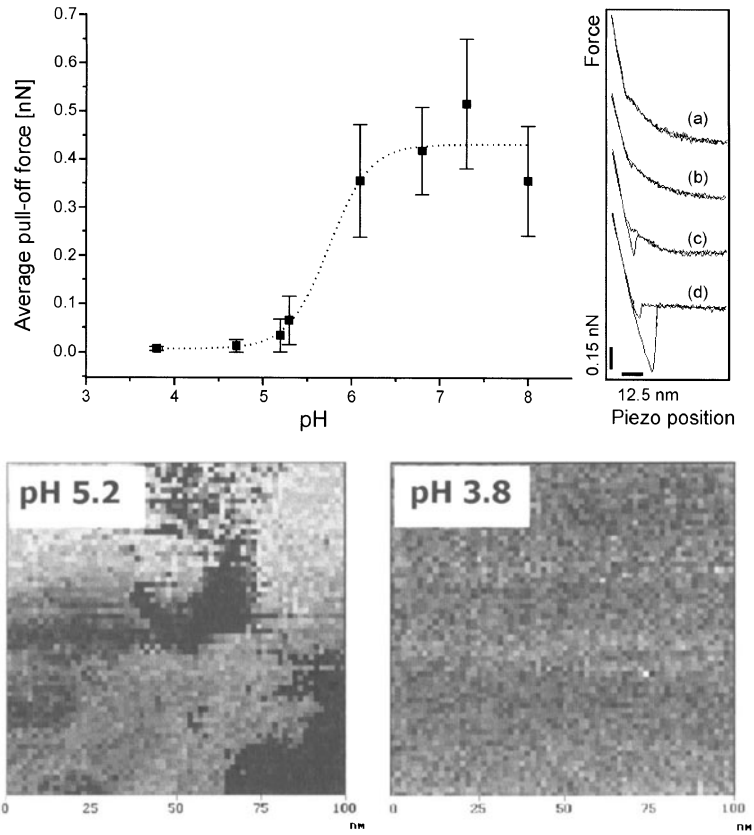

Fig. 27 *Top*: Force titration of plasma polymerized allylamine film (the *dotted line* has been added to guide the eye). To the right corresponding force-distance curves which display (depending on the pH of the buffered aqueous solution) (a) exclusively repulsive (pH 4.7), (b) and (c) repulsive and attractive (pH 5.3 and pH 6.2, respectively), or (d) exclusively adhesive interactions (pH 6.8). Bottom: FV images of corresponding plasma polymerized allylamine film at pH 5.2 (bright 0.0 nN, dark − 2.0 nN) and pH 3.8 (bright 0.0 nN, dark − 0.1 nN). (Reprinted with permission from [57]. Copyright 2000 American Chemical Society)

CFM using hydroxy- or methyl-terminated tips has been used to investigate the frictional properties of polystyrene films exhibiting different degrees of oxidation, ranging between 0–20 at. % oxygen by XPS [188, 189]. It was claimed that absolute friction values of the oxidized surfaces could be derived, if the torsional response of the tip cantilever and the resulting signal output of the photodiode were known. A linear increase in the coefficient of friction with increasing surface oxygen level (by XPS) and in the water contact angle were observed. The friction values of the oxidized surfaces obtained using the hydroxy-terminated tip were higher than those obtained using the methyl-terminated tip. It was suggested that this could be used

to follow approximate changes in polar free surface energy of polymer surfaces due to oxidation. Moreover the lateral resolution using this CFM approach was demonstrated using a model system consisting of a PS/PMMA blend. Little image contrast was obtained using an non-functionalized or a methyl-terminated tip since the friction difference between the two phases was too low (Fig. 28a). Using a hydroxy-functionalized tip a clear contrast was obtained, thus the increased friction contrast was chemical in nature and caused by an increased polar interaction between the tip and surface (Fig. 28b) [188].

Eaton et al. used FV mapping for imaging of a phase-separated blend of PMMA and poly(dodecyl methacrylate) (PDDMA) [190, 191]. Unmodified silicon nitride cantilevers were used in ambient conditions in air or in water using a liquid cell. Differences in pull-off forces correlated with features in topography, making it possible to distinguish between the PDDMA-rich

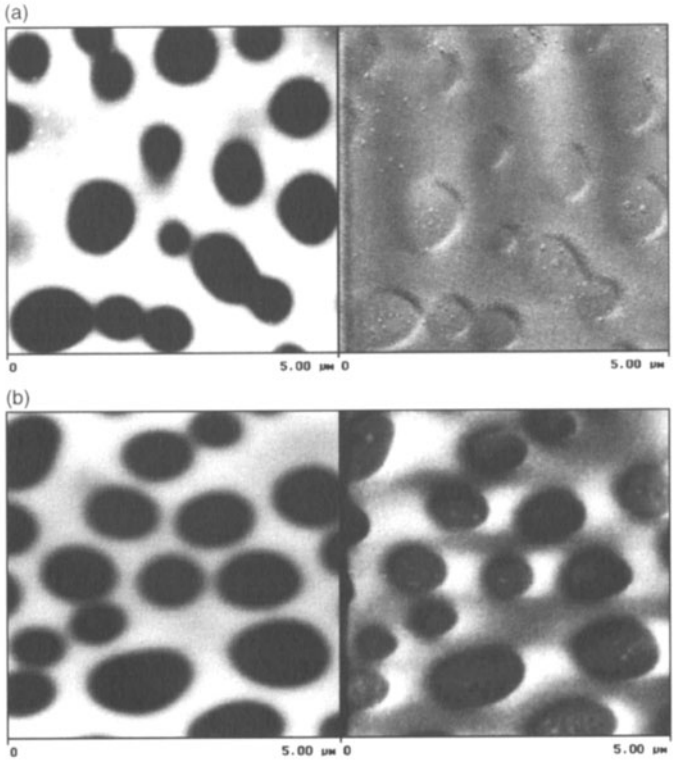

Fig. 28 Topographical (*left*, z range 150 nm) and frictional force (*right*, z range 0.2 V) images of a PS/PMMA blend using unfunctionalized (**a**) and hydroxy-terminated (**b**) tips. The continuous phase consists of PMMA. (Reprinted with permission from [188]. Copyright 2000 American Chemical Society)

domains (exhibiting higher adhesion) from the PMMA-rich domains (exhibiting lower adhesion). However, since the values of the adhesive force measured in the PDDMA-rich domains were lower than those determined for films of pure PDDMA, it was suggested that this was due to sub-micrometer-level domains of PMMA, even though no evidence for this hypothesis was provided. Particularly high adhesion forces were observed at the interface between the domains, originating from the increased contact area between the tip and the substrate [191]. It was suggested that indentation mapping, using a stiffer cantilever, could be used as a complimentary technique to the adhesion mapping, since it was less dependent of topographic features.

By performing adhesion mapping and friction force imaging of mechanically scratched structures on biaxially oriented polypropylene films with a conventional Si_3N_4 tip an increase in surface energy of the scratched regions was observed [192]. This was explained in terms of increasing density and orientation of polymer strands, as well as added energy by the work done by the mechanical scratching. The increase in the surface energy ("adhesion force") was comparable to that introduced by surface oxidation of the unscratched surface after 1 min UV/ozone exposure. The CFM approach was thus successfully used to create and assess local active sites of the surface in terms of surface energy increase or wettability improvement.

Furthermore, CFM was used in a study on the surface chemical properties of UV excimer laser irradiated polyamide to complement XPS and ToF-SIMS data [193], as well as in a study on the surface properties of modified poly(dimethyl siloxane) (PDMS) [194]. The surface hydrophobicity of UV/ozone-treated PDMS was also probed by Hillborg et al. using CFM and AFM indentation measurements, among other techniques, as a function of storage/recovery time [179]. The CFM data were acquired in the form of force volume images and were converted automatically into pull-off force images and the corresponding histograms (force distributions) using a custom-made software. Exposure times < 30 min resulted in laterally homogeneously oxidized surfaces, which are characterized by an increased modulus and a high segmental mobility of PDMS. As detected on a sub-50 nm level, the subsequent "hydrophobic recovery" was characterized by a gradual increase in pull-off forces and a decrease in normalized modulus, approaching the values of unexposed PDMS after 8–50 days. Longer exposure times (60 min) led to the formation of a hydrophilic silica-like surface layer. Under these conditions a gradual surface reconstruction within the silica-like layer occurred with time after exposure, where a hydrophilic SiOx-enriched phase formed < 100 nm sized domains, surrounded by a more hydrophobic matrix with lower normalized modulus (Fig. 29).

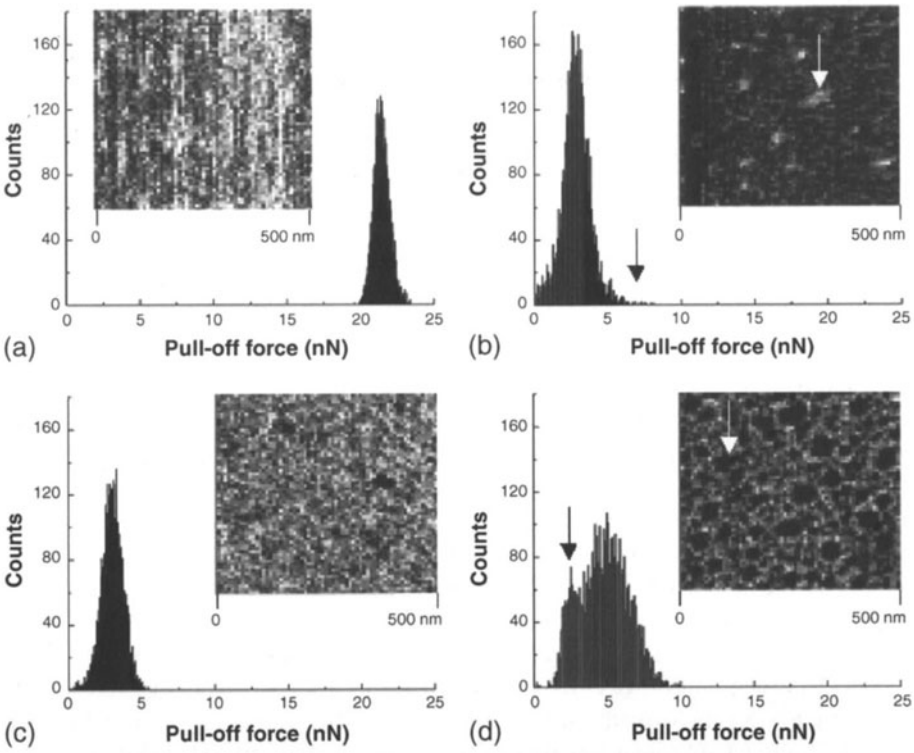

Fig. 29 Representative histograms of the pull-off forces and corresponding adhesion (pull-off force) images of: (**a**) unexposed PDMS and oxidized PDMS; (**b**) 0.1; (**c**) 8 and (**d**) 40 days after exposure to 60 min UV/ozone. In the adhesion images, the *gray scales* are individually scaled from dark (low pull-off) to bright (high pull-off). (Reprinted with permission from [179]. Copyright 2004 American Chemical Society)

6 Other Techniques to Image Chemical Functional Groups and their Lateral Distributions

In this section surface characterization techniques, which are capable of lateral imaging of polymer surfaces with sub micrometer resolution, are discussed. The following terms will be used: mapping is used when small regions of a single area of interest are sequentially sampled. These regions are then linked together via their spatial coordinates. The term imaging is used when the whole area of interest is sampled simultaneously, and the localized spatial resolution is achieved by other means [195].

6.1 Secondary Ion Mass Spectrometry

SIMS is based on the mass spectrometric analysis of secondary ions, generated by the interaction of a primary ion beam (usually Ga^+ or Ar^+) with the polymer surface. The emitted fragments of the molecules allow characteristic signatures of elements, isotopes and molecules to be identified. Generally, ToF analyzers are used due to their higher sensitivity, compared to quadrupole detectors. Of the currently available spectroscopic imaging techniques for non-conducting materials, time-of-flight secondary ion mass spectrometry imaging is a powerful method thanks to its combination of high sensitivity (femtomole-attomole), capacity to detect molecules as well as elements, and sub-micrometer lateral resolution [196–199]. There are two operational regimes in SIMS, which yield fundamentally different information and analytical features. The so-called dynamic SIMS involves use of a high primary ion current density on the sample that allows fast erosion so that in-depth concentration profiles can be measured. Static SIMS operates in principle the same primary ion guns, but at a lower primary ion current ($< 10^{13}$ ions cm^{-2}), where the basic idea is that each local environment in the sample is hit only once by the primary beam, thereby only acquiring data from the top 10–20 Å [196–199]. SIMS imaging can either be performed using an ion microscope or ion microprobe instruments [197, 198]: the ion microprobe uses a finely focused primary ion beam, which is raster-scanned point by point over a given area. The intensity of a given ion or a full mass spectrum is then acquired from each point. In the ion microscope mode, the entire area is irradiated by a less focused primary ion beam. The lateral distribution information is then obtained by the use of special ion optics and position-sensitive detection. Using the microprobe mode, the lateral resolution is defined by the beam diameter (around 20 nm using liquid metal ion guns) [198, 200]. In the microscope mode the lateral resolution of approximately 0.4 μm is determined by the ion optics of the instrument [197]. The drastically decreased sputter and ionization yield of secondary ions for higher molar mass polymers, however, reduces the lateral resolution compared with these values obtained at favorable conditions (single layers of molecules etc.) [197]. Thus, in imaging polymer surfaces a higher intensity, especially for the higher mass molecular peaks, in order to allow molecular imaging with the most characteristic ions, and shorter exposure times are desirable. The best theoretical resolution (Δl) is correlated according to the following equation:

$$\Delta l = \sqrt{\frac{\sigma}{Y}} \tag{34}$$

where σ is the damage cross section of the exposed surface layer and Y is the yield of secondary ions (the number of detected secondary ion species divided by the total number of applied primary ions). In this context, post-

ionization (of emitted neutral particles) techniques for molecular species and new primary ion beams in order to increase the yield are promising for the future development of SIMS. [197, 198, 201–204] Static SIMS imaging using cluster ion beams (for example Au_2^+) generated with a liquid metal ion source seems to be a promising approach for imaging organic surfaces [204].

Typical applications of imaging SIMS to polymers are characterization of Langmuir–Blodgett (LB) films [205, 206], self-assembled monolayers [207], polymer blends [208] and micro patterned surfaces [209, 210]. Molecular identification of active members of bead-bound combinatorial libraries is another application well suited to imaging SIMS. Femtomol quantities of different peptides attached to 30–60 μm PS beads have been determined [211, 212], even though the method provides fewer structurally informative fragments, compared to MALDI-MS [212]. At least two factors limit the spatial imaging of self-assembled monolayers and polymers as identified by a number of researchers [42, 202, 210, 213, 214]: firstly, organic molecules do not frequently give rise to unique molecular ions with an intensity that is sufficiently large to permit imaging below the static SIMS limit. Secondly, low mass atomic ions often have high enough intensity for ToF-SIMS imaging under static conditions, but can originate from different chemical species on the surface, ranging from the underlying substrate, as well as from other organic moieties. One solution to this problem is the use of specific labeling techniques, for example using isotopes [208, 215]. Stable isotope labeled proteins (^{15}N-labeled streptavidin) were utilized in ToF-SIMS imaging of biotin micro-patterns on polymer or gold surfaces. The imaging was based on the specific secondary ion ($C^{15}N^-$).

Leufgen et al. demonstrated the use of static ToF-SIMS to visualize two coexisting phases in LB films, prepared as a mixture of two fluorescent dyes: NBDPC and DPPC (nitrobenzooxadiazol- and dipalmitoylphosphatidylcholine) [216]. Images of the monolayer produced by mapping the detected intensities of specific secondary ions are shown in Fig. 30. The lateral resolution was approx. 1 μm. The distribution of the protonated molecular ions of NBDPC was enriched in a liquid-expanded phase (Fig. 30a), whereas the protonated DPPC molecular ions were enriched in the liquid-condensed phase (Fig. 30b). The domain structures seen in the images of the protonated molecules corresponded exactly to fluorescence data (not shown). The homogeneous distribution of the gold substrate ions is shown in Figure (Fig. 30c).

Bourdos et al. observed that the contrast of ToF-SIMS images of LB films was generated not only by chemical, but also by physical differences within the film on the substrate (packing of molecules in the liquid crystal phase) [206]. The lateral resolution obtained during the experiments was approximately 230 nm. The resolution was limited by the pixel raster used even though the physical limit determined by the ion beam was approximately 80 nm.

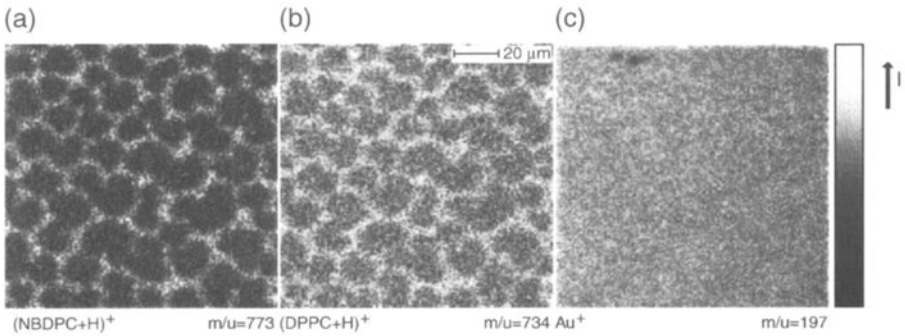

Fig. 30 Mass-resolved images by static TOF-SIMS ($120 \times 120\ \mu m^2$). The secondary ion intensities are color coded, from dark to bright. Illustrated is the lateral distribution of the molecular ions of: (**a**) NBDPC, (**b**) DPPC, and (**c**) gold ions (substrate). (Reprinted with permission from [216]. Copyright 1996 American Chemical Society)

Static ToF-SIMS imaging of the morphology and miscibility of ethylene-tetrafluoroethylene copolymer/PMMA blends was successfully performed using the ion F^- ($m/z = 19$) as a distinct characteristic fragment. The lateral resolution was approx. 780 nm [217]. The corresponding images showed that slow cooling facilitated the phase separation between ETFE and PMMA domains. The dynamic rearrangement of bromine end groups ($^{79}Br^-$, $^{81}Br^-$, $m/z = 79, 81$) attached on amorphous or semi crystalline polymers prepared by condensation polymerization of Bisphenol A and 1,8-dibromooctane was investigated using static ToF-SIMS [218]. The images revealed that the bromine end groups were preferentially expelled to the surface of the lamellae during the crystallization process.

Static ToF-SIMS was also used to investigate the effects of various surface-engineering conditions on the lateral distribution of poly(L-lysine)- or poly(ethylene glycol) modified poly(lactic acid). However, the analysis of poly(ethylene glycol) and poly(lactic acid) surfaces did not produce distinguishing ions of a sufficient intensity, yielding high enough lateral contrast. During these conditions, imaging XPS (Sect. 6.2) was successfully used despite of the comparatively low lateral resolution (25 μm, compared to approx. 1 μm using SIMS) [219]. This combination of instruments was also successfully used for chemically micro-patterned surfaces, formed by plasma-polymerization [209]. Distinct regions of fluorine, carboxylic acid and hydrocarbon functionalities were imaged by ToF-SIMS, whereas mapping XPS was used to image the nitrogen content (using the N 1*s* peak) due to the lack of a unique nitrogen signal of allylamine [209]. Another application of imaging static ToF-SIMS described in literature is the characterization of surface diffusion of polymers on inorganic substrates [220]. It was observed that PS and PMMA did not exhibit any surface diffusion at room temperature, whereas poly(dimethylsiloxane) and a perfluorinated polyether exhibited high surface

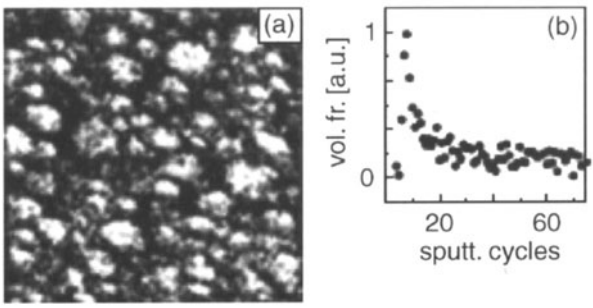

Fig. 31 Imaging by dynamic SIMS ($27 \times 27\ \mu m^2$): (**a**) deuterated polystyrene (*white areas*, $m/z = 26$) distribution in a deuterated polystyrene/polyimide (50/50) blend; (**b**) corresponding profile of the polyimide fraction as function of distance from surface (1 sputtering cycle ≈ 0.5 nm). (Reprinted with permission from [208]. Copyright 2001 Wiley-VCH)

diffusion. Provided that a well-defined boundary between a covered and uncovered surface area can be produced, this technique can be applied to a wide variety of substrate-overlayer combinations [220].

By using dynamic mode SIMS the lateral distribution of phases in three dimensions can be resolved (Fig. 31). Thin films (thickness ca. 500 nm) of binary mixtures of deuterated or partially brominated PS, polyisoprene and poly(vinylpyridine) were investigated with a lateral resolution of approximately 120 nm and composition versus depth profiles with a resolution better than 10 nm [208]. The brominated PS formed continuous phase-domain structures in the interior of the films whereas they were encapsulated by deuterated PS layers at the interfaces. Moreover a very thin layer (ca. 3 nm) of polyisoprene covered the surface of a binary mixture of poly(isoprene)/deuterated PS [208].

Dynamic SIMS has also demonstrated the clustering of oxidized poly(pyrrole) into small granules (50–300 nm) embedded in a matrix of ferric stearate LB films after exposure to pyrrole vapors [221], and the surface enrichment of fluorinated chains in a poly(methyl methacrylate) matrix [222].

6.2 X-ray Photoelectron Spectroscopy

XPS is one of the most popular spectroscopic methods for surface analysis of polymers. It provides qualitative and quantitative information on the atomic composition down to a depth of typically 0.5–10 nm depending on the take-off angle. In an XPS instrument the sample is positioned in a high vacuum chamber and is irradiated with a monochromatic X-ray source (generally Al K_α or Mg K_α) resulting in an emission of photoelectrons from the exposed surface region. The XPS spectrum shows the number of photoelec-

trons as a function of their kinetic energy, which is characteristic of the element and its binding state (except for helium and hydrogen). The recent increase in instrumental sensitivity has led to the development of spatially resolved XPS [223, 224]. The spatial resolution of commercial instruments is in the order of 5–30 μm with acquisition times of minutes rather than hours [223, 225]. The lateral resolution is limited mainly due to the difficulty in focusing the X-ray beam. Although XPS imaging does not have the same spatial resolution as ToF-SIMS, the advantage of XPS is not only the determination of the atomic surface composition, but also the information it delivers on the electronic environment (often referred to as chemical shift) in a non-destructive manner [209, 219]. As is the case with SIMS, imaging can be made using two different main techniques: the first utilizes the X-ray beam to bombard the specimen very locally, i.e. an X-ray probe. The second method floods the specimen with X-rays and then images parts of the surface by manipulating the photoelectrons in a controlled manner [225].

A direct comparison of the spatial resolution of XPS and transmission infrared spectroscopy imaging on heterogeneous polymer blends of poly(vinyl chloride)/PMMA was presented by Artyushkova et al. [226] The spatial resolution of the XPS and infrared instruments was 2–3 μm and 7 μm, respectively. The comparable resolution of the instrumentation allowed for images and spectra from the same areas of the samples to be directly compared (Fig. 32).

The XPS image was based on the intensity of the Cl 2*p* peak, whereas the infrared image was based on the absorption at the band at 1333 cm^{-1}, used for identification of PVC. The PVC enriched (bright) areas in the images were

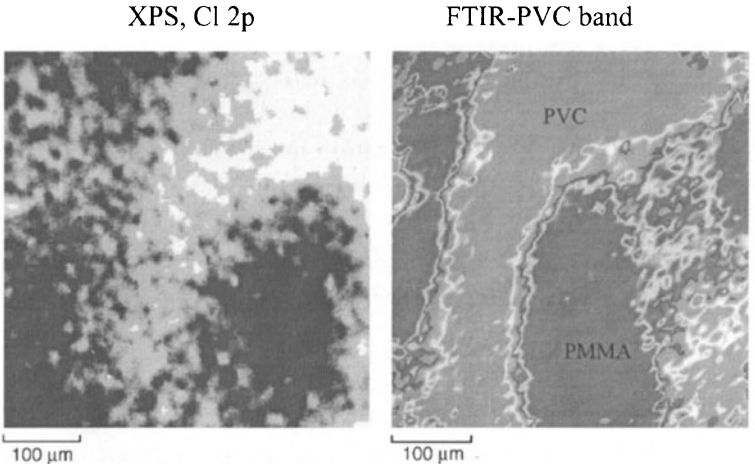

Fig. 32 Comparison of XPS Cl 2*p* and transmission FT-IR PVC (1333 cm^{-1}) images for a PVC/PMMA (25/75) blend. (Reprinted with permission from [226]. Copyright 2000 Society for Applied Spectroscopy)

similar in both shape and size. Since the XPS sampled approximately the top 10 nm, while the transmission infrared images were representative of the total film thickness (a few micrometers). This implied that the phase-separated regions extended well into the film (Fig. 32). This combination of different techniques thus provided a more complete method for characterizing complex polymers containing different surface and bulk combinations [226].

Owing to the sensitivity of the chemical surrounding, XPS imaging was used to study segregation effects of polyethylene glycol (PEG)-modified polylactic acid (PLA) systems, since it enabled a straightforward distinction of the two species [219]. Mapping of the signal intensity at a given binding energy (C 1*s*) as function of the position along a sample surface was performed with a lateral resolution of approx. 25 μm. The PLA generated three peaks each being separated by binding energy shifts of approx. 2 eV and 4 eV relative to the C 1*s* methyl group at 285.0 eV. The C 1*s* ether peak of PEG arose at 286.3 eV, enabling a straightforward deconvolution and determination of the relative intensities of the two polymers. The method was used to assess surface segregation of PEG and PLA, which were of the order of tens of microns [219]. Moreover imaging XPS and laterally resolved Raman microscopy were used to investigate the effects of laser-induced ablation of polyimide [227]. Both methods revealed the deposition of carbon surrounding the ablation craters (300 μm diameter).

Although spatially resolved XPS is constantly improving (increased intensity of the X-ray source, improved electron optics of the lenses, increased transmission of the energy analyzer) it is believed that SIMS will be at an advantage for probing inhomogeneous surfaces [225]. However, when the chemistry involved in the surfaces is complex, XPS offers unique capabilities owing to the chemical shifts in binding energies [225].

6.3 Matrix-Assisted Laser Desorption/Ionization Mass Spectrometry

Matrix-assisted laser desorption/ionization mass spectrometry (MALDI-MS) based imaging was first described in 1995, developed as a detection method for thin-layer chromatographic separations [228]. The images are obtained by acquiring mass spectra stepwise over the desired area of a surface. The mass of the ions of interest is then extracted and displayed at their correct spatial positions to produce the final image. The spatial resolution achieved was 250–500 μm even though the ultimate spatial resolution, based on matrix heterogeneity and minimum laser beam diameter to acquire a good signal intensity, was estimated to be in the order of 50 μm [228]. The spatial resolution of the imaging approach is moreover limited by the physical ability to focus and step the laser across the sample, spreading of the sample due to the addition of the liquid matrix, [228, 229] as well as by the software used for the scanning and acquisition process [230]. The capability of imag-

ing MALDI-MS has been demonstrated by the acquisition of mass spectra images of symbols printed by an ink-jet printer with a lateral resolution of 30 μm [230, 231]. Two letters were printed on top of each other using different inks [230]. Since the inks differed in molecular weight, the letters did not interfere with each other in the acquired images (Fig. 33). Moreover

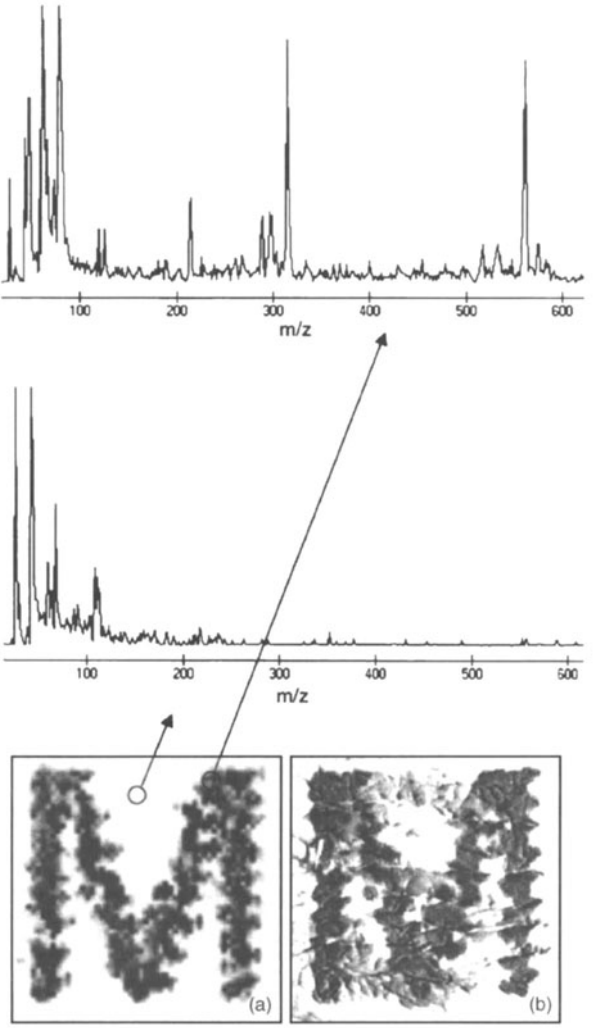

Fig. 33 (**a**) Mass spectrometry image ($m/z = 340$) by MALDI and (**b**) optical image of a letter printed with an ink printer. The size of the images are $1500 \times 1500\ \mu m^2$. (Reprinted by permission of Elsevier Science from "Automated mass spectrometry imaging with a matrix-assisted laser desorption ionization time-of-flight instrument", by Stoeckli et al., Journal of the American Society for Mass Spectrometry, Vol. 10, pg 69, 1999, by the American Society for Mass Spectrometry)

the potential to perform quantitative analyses was demonstrated [230]. Since MALDI-MS imaging offers the possibility to detect significantly higher molar masses than SIMS, direct MALDI-based imaging is believed to become an important complement to other molecular imaging techniques [229].

6.4 Raman Microspectroscopy

Raman microspectroscopy is based on an optical microscope, where the spectral distribution of inelastically scattered light is detected by a Raman spectrometer/CCD detector, thereby microprobing an area with a spatial resolution of about 1 μm. The spatial resolution of Raman systems employing normal optical microscopes is limited to approximately the wavelength of the light (about 0.5 μm), because both the illuminating laser light and the Raman scattered light are collected in the optical far field (i.e. many wavelengths of light away from the scattering material). While the methods of image acquisition are diverse, each generates a two-dimensional map based on the intensity of a given Raman scattering band. By using Raman imaging, a widened laser beam provides a global illumination of the investigated area which is then imaged directly onto a CCD detector. A complete Raman spectrum can be collected for each pixel. Raman mapping is an equivalent procedure which uses point illumination to obtain the spectrum at single points, gathered in a grid pattern over an area of the sample. The addition of confocal filters can increase the lateral resolution and allows one to image at different depths. The theoretical performance of a confocal Raman microscope is mainly determined by the optical properties of the microscope objective (numerical aperture, magnification power, and focal length) and by the size of the pinhole placed in the back image plane of the microscope [232]. The depth of analysis in the confocal mode is in the order of 2–4 μm [232]. Recent developments in Raman spectrometers have led to great improvements in sensitivity and imaging capabilities [233, 234], allowing mapping of polymer surfaces with a lateral resolution of < 1 μm [235, 236]. Submicron spatial resolution using wide-field Raman imaging in the confocal mode has been demonstrated by imaging polystyrene spheres (2 μm diameter) with an interparticle distance of 200 nm [237]. The dominant criteria to take into account when obtaining a Raman image is the weakness of the Raman effect [234, 237]. Since the incident laser energy is focused on a very small area, low laser power must also be used to minimize local thermal expansion and sample degradation [237]. Moreover problems of sample fluorescence and photodamage may occur when mapping polymer surfaces [236, 238, 239]. Markwort et al. compared Raman imaging using global illumination with mapping by point illumination and concluded that lower spectral resolution, increased fluorescence and artifacts caused by sample shape were worse for the global illumination method [240]. These authors recommended the use

of point illumination with confocal light collection for the study of heterogeneous polymer surfaces.

A polypropylene/polyethylene copolymer containing a small amount of blended ethylene-propylene rubber (EPR) was characterized by confocal Raman microspectroscopic mapping with a spatial resolution of 1 μm. The surfaces exhibited micrometer-size domains with a higher content EPR in the copolymer matrix (Fig. 34a). However, since absorption bands originating from the copolymer were more or less dominant in all spectra, it was concluded that the EPR existed as submicrometer particles. Figure 34 shows the same surface after a surface modification by exposure to an argon-plasma. The regions containing higher amounts of EPR exhibited a slight increase in number and size suggesting that the EPR was less susceptible to damage due to its crosslinked nature [235]. Due to the poor sensitivity of Raman spectroscopy to polar functional groups it was not possible to map the oxygen functionality on the surface. However, by mapping using reflection infrared spectroscopy the presence of hydroxy groups was verified. The lateral resolution was, however, limited to 30–50 μm. After the plasma treatment, the surfaces were grafted using polystyrene. The lateral distribution of polystyrene was shown to be heterogeneous and corresponded to the areas of higher EPR concentration after the plasma treatment [235].

By combining Raman imaging with photoacoustic FT-IR and FT-IR microscopy three-dimensional maps of the heterogeneous degradation of epoxy and polyurethane films exposed to UV and water vapor were obtained [241]. Similarly, the phase separation in styrene/butylacrylate copolymers and latex films were analyzed [242]. Blakey and George used point illumination Raman mapping to investigate the surface of photooxidized PP with a lateral resolution of 1 μm and successfully mapped the distribution of both oxidation products (α,β-unsaturated ketones) and catalyst residues [239]. The distri-

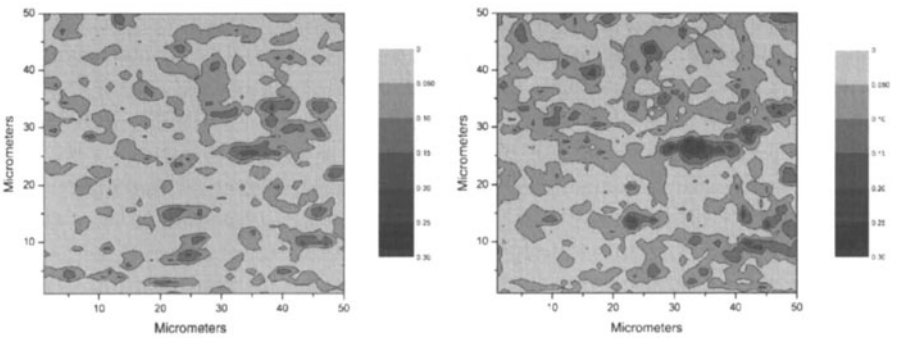

Fig. 34 Raman map of the surface distribution of EPR in a PP matrix (**a**) before and (**b**) after plasma treatment (the absorption band used for EPR was 1064 cm^{-1}, whereas 1220 cm^{-1} was used for PP). (Reprinted with permission from [235]. Copyright 2001 Society for Applied Spectroscopy)

bution of the oxidation products did not correlate with the distribution of the catalyst. It was suggested that the catalyst residues tended to stabilize the polymer in the immediate vicinity, but also formed reactive species that diffused away from the catalyst to initiate oxidation [239].

Raman confocal microprobe mapping was used to investigate the effect of a silica filler on the phase separation in binary blends of brominated poly(isobutylene-*co*-*p*-methylstyrene) and *cis*-1-4-polybutadiene with a lateral resolution of less than 1 μm [238]. The size of the polymer domains were less than one micrometer, even though some domains formed aggregates, which in some cases exceeded 5 μm. By using long (70 μm) linear scans the average size of these aggregates as a function of added silica filler was investigated. Using linear scans are less time consuming, but provide similar information. It was found that the average size of these aggregates decreased with increased concentration of silica: from 4–6 μm without silica, down to 2–2.5 μm at 45 phr (parts per hundred) silica as a result of the increasing shear deformations during the internal mixing process.

By using Raman imaging/mapping techniques with a lateral resolution of 1–2 μm inhomogeneous surface structures of a number of polymers were investigated including sub-microdomain structures of polycarbonate/poly(styrene-*co*-acrylonitrile) blends [243], recrystallization of polyethylene blends [244], surface architecture of a chlorinated PP-primer in thermoplastic olefins [245], the effect of embedded PET fibers on the orientation of PP spherulites during crystallization [246], surface ablation/carbonization of polyimide by laser irradiation [227] and characterization of photoablated PET surfaces [247]. Furthermore, the chemistry and kinetics of holographic grating formation in a multicomponent photopolymer was also studied to directly image the submicron concentration variations responsible for the hologram diffraction [236].

An interesting approach describing the combination of the lateral resolution of near-field scanning optical microscopy with Raman spectroscopy to attempt material-specific surface characterization on the nanoscale [233, 248, 249]. However, long acquisition times (approx. 10 h) and attendant instrumental drift severely limit the advantage in resolution [250]. A strongly increased Raman signal from molecules attached to metallic nanostructures have attracted considerable attention since this effect, referred to as Surface Enhanced Raman Scattering (SERS) shows promise in overcoming the low-sensitivity problems inherent in Raman spectroscopy [251, 252]. Surface-enhanced Raman mapping has been used to produce images of patterned self-assembled monolayers of molecules, differing only in the terminal functional groups, on silver or gold surfaces with a resolution of approximately 2 μm [250, 253, 254]. The technique combines chemical selectivity with the ability to be used under ambient conditions or even in the presence of a liquid, as in an electro-chemical cell containing an aqueous electrolyte [250].

6.5
Near Field Scanning Optical Microscopy

Near field scanning optical microscopy (NSOM) is a scanning probe microscopy technique, which can simultaneously collect nanoscale topographic and fluorescence images by scanning with a force feedback mechanism in the near-field using a fiber optic probe with a sub-wavelength aperture. Thus this technique is not diffraction limited, which allows one to obtain optical (spectroscopic) information in the sub-wavelength length scale. In a region very close to the aperture, there is an evanescent electric field, whose lateral extent is confined by the size of the aperture, which is typically on the order of 25–150 nm [255, 256]. By keeping the sample-probe separation constant within this near-field region (approx. 7–15 nm), an image of the sample is formed with a resolution of $\sim$ 100 nm. The NSOM probe is used to excite the sample and the transmitted light or the excited fluorescence is collected together with topographic data in either transmission or reflection mode. Absorbance and fluorescence spectroscopies provide detailed chemical information while polarization spectroscopy can be used to determine molecular orientation. An important consideration in reflection NSOM is the effect of contributions to the signal from the bulk of the samples. However, the evanescent modes of the NSOM tip will only excite the sample to a depth of approximately 100 nm giving NSOM its surface sensitivity [257].

The application of NSOM to characterization of polymer surfaces has been so far mainly limited to thin conjugated polymer films [255, 257–266]. Spectroscopic studies have revealed strong heterogeneities in the emission from these films [255, 257, 260], while others have observed a homogeneous emission [266]. A direct correlation between the nanometer-scale topography of a conjugated polymer film and the local electronic properties was found by NSOM: thin films of poly(*p*-phenylene vinylene) exhibited polymer aggregates in the size of 100–200 nm, which correlated to areas with lower photoluminescence (Fig. 35) [257, 262]. Furthermore thin films of substituted polyfluorene also exhibited polymer aggregates in the size of 50–150 nm, which correlated to regions with lower fluorescence [255, 259, 260]. It was suggested that these aggregates were caused by partial insolubility of the polymer in solution prior to casting [255, 259, 260]. It is believed that these aggregated species may be responsible for the reduced fluorescence efficiency of polymeric light emitting devices (LEDs) [264].

However, when thin films of a substituted poly(*p*-phenylene vinylene) were studied by NSOM no aggregated domains above the resolution limit of 50 nm were found [266]. With careful evaluation of both the spectroscopy and morphology using NSOM, new polymers with superior properties for improved device performance can be created by tailoring the molecular structure in order to avoid aggregation [259, 260, 264, 265].

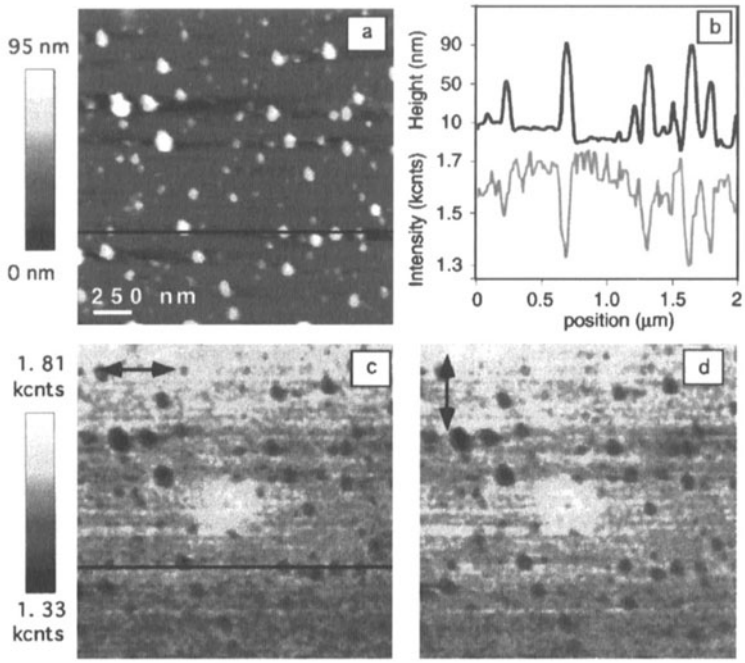

Fig. 35 Near field scanning optical microscopy (NSOM) images ($2 \times 2\ \mu m^2$) of a thin conjugated polymer film: (**a**) topography, (**b**) line scans of lines shown in (**c**) and (**d**), (**c**) and (**d**) NSOM fluorescence images at orthogonal polarizations. (Reprinted with permission from [45]. Copyright 2000 American Chemical Society)

NSOM has also been used to pattern thin polymer films with resolution below 100 nm by photo-oxidation [262]. Moreover, time-correlated single photon counting has been successfully integrated with NSOM to image chemical species with different fluorescence lifetimes with a spatial resolution of < 100 nm [267]. The method was used to follow a photochemical degradation of a thin conjugated polymer film [267]. In addition, infrared absorption spectroscopy has been successfully integrated with NSOM for the analysis of polymer surface phenomena [268, 269]. The chemical specificity of infrared spectroscopy, combined with near-field sub-wavelength resolution was used to characterize transport phenomena in a polymeric photoresist during a UV-lithographic process [268].

7 Outlook

Based on the current state of the art, as reviewed in this article, it is obvious that much work needs to be done in order to approach surface analysis of

polymers with true nanometer scale spatial resolution combined with exact chemical information. For crystalline solids, in an ideal (ultrahigh vacuum) environment great progress has been made following the advent of related real-space imaging techniques, such as the scanning tunneling microscope (for metals and semiconductors). In such cases true atomic (or sub-atomic) information in direct space can be obtained on the sub-nanometer scale. These ordered systems can also be successfully studied down to the atomic level by high-resolution transmission electron microscopy. Polymers, unfortunately, exhibit in general a very complex structural hierarchy and the degree of order typical for inorganic and metallic crystals is virtually unknown in the world of macromolecular systems. The complex structural architecture is obviously reflected also by the surfaces and interfaces of these materials. In addition, due to the large size molecular building blocks the definition of surface as such is not that straightforward as it is for e.g. metallic crystals.

AFM-based approaches for high resolution lateral mapping of the surface chemical composition of polymers have made their debut, expanding resolution limits in favorable cases down to the 20–30 nm level. These approaches, which exploit the use of chemically functionalized tips, can be considered relatively mature in terms of mapping differences in surface and interfacial energies (hydrophilic/hydrophobic) in the sub-micrometer to sub-100 nm regime on flat polymer specimens of known origin or treatment. However, the chemical information is still indirect and limited, and does not match in quality the exact composition information provided on the ensemble average level (without high spatial resolution) by established spectroscopic and spectrometric methods.

The question can be posed: can the problem of exact and accurate surface analysis of polymers be solved and if yes, when? This problem has two facets: a principal, theoretical one, and an experimental, instrumental one. A full theoretical solution means that the problem is solved, when the position and type of each particle (atom) in space and time at (or near) the surface would be known. Problems like this, including the description of atomistic and molecular systems with a high degree of freedom, are treated by statistical mechanics. There are practical and technical problems with an exact atomistic description, including the amount of information and the amount of data that is absolutely necessary. Statistical mechanics treats systems with a high degree of freedom by various means over partition functions for the different ensembles. For such a description the surface must be first defined. As a pure geometrical definition for non-crystalline materials (polymers) is not possible, one option is to define surfaces to within a given depth of field by the technique used to measure composition. For example, surface tension is sensitive to the few top molecular (or atomic) layers due to cutoff in effective pair interaction functions, while XPS (depending on the escape depth and electron take off angle) can look into the surface to a thickness of up to 10 nm, and infrared reflection spectroscopy for surface characterization gathers informa-

tion from a top surface layer with a few to 10 μm depth. For validation of statistical averaging structural information (on the ensemble level) is usually used in the Fourier space. In this review we focused on direct space imaging and direct space local determination of structural heterogeneities, and left surface scattering out from our treatment. For the average description of surfaces the relationship between these two approaches still needs to be established.

If we set out to unravel surface chemical functionalities with high spatial resolution down to atomic detail, we also encounter various practical (technical) problems. It is fair to say that the technique development for direct space analysis (again, we exclude Fourier space methods) is still lagging much behind. Chemical force microscopy can be considered as a first step in the direction of a true description of surface chemical functionalities with high spatial resolution in polymers, primarily based on the chemically sensitive analysis of AFM data via adhesion mapping. At this point the detailed theory for force spectroscopy is not developed beyond the description of London forces. The consideration of the effect of polar functional groups in force spectroscopy (similar to difficulties with solubility parameter and surface tension approaches for polar forces, as well as specific interactions) is still in its infancy. Instead, one must still rely on continuum contact mechanics to couple measured forces and surface free energies.

Clearly, the briefly reviewed complementary spectroscopic techniques are important to approach these current shortcomings in a rational manner for practical purposes. For future progress significant technical refinements for, e.g. XPS and SIMS imaging, will enhance the spatial resolution and will lead to new opportunities. However, the costs for the equipment and instrumentation may limit the widespread application of these approaches compared to AFM-based techniques.

So far we have not considered surface dynamics and time-dependent relaxation processes. These can alter surfaces and thus time averaging must also be considered. At the same time, the speed with which the different approaches gather information about lateral distributions of surface chemical groups must be recognized. Finally, another very essential variable is the chemical environment (solution, gases, etc.). For ionizable surfaces to describe their stability and lateral chemical structure, domain stability of charged heterogeneous patches (usually different from the bulk), differences in ionization behavior, conformational changes and molecular relaxation, which drive dynamic surfaces towards different equilibria in different mediums, must be considered.

It is of course difficult to predict future developments, however, a number of directions can be identified. These comprise the development of the next generation force microscopy instruments (advanced analysis of the behavior of resonating levers), which would deliver topological, physical, as well as chemical information on surfaces in a parallel fashion, with high reso-

lution, fabrication of smaller, sharper probe tips (to increase the resolution and attainable scan rates, with more robust chemical functional coatings), manufacturing small probes with high resonance frequencies and using them with fast and robust electronics to increase imaging speed and systems for robust imaging under full environmental control. These developments will likely lead to a significant broadening of the possible applications and attainable lateral resolutions, which in turn will allow one to bring many more systems and approaches from the academic level to everyday routine, which is of relevance for the practitioners in industry and R&D. This anticipated development must be complemented by simultaneous theoretical advances to enable one to tackle problems with increased complexity. Corresponding developments will likely be complemented by the advancement of other techniques, such as those briefly mentioned, as well as others, which possess the potential to provide new, complementary information about chemistry on the nanoscale.

Acknowledgements The idea of this review was born at the IUPAC-MACRO Warsaw meeting in 2000 during a conversation between Prof. H. Kausch and the first author of this review. It took us more than three years to eventually complete the final version. Among the many reasons, our ongoing continuing work in this area posed new challenges, which we wanted to tackle prior to finishing up this overview. The patience, great help, most useful feedback and encouragement by Henning Kausch during this process were instrumental. Without this the review would not have been written. Help and attention by the Springer staff was also very important and is highly appreciated. Ms. Cindy Lammertink made very essential contributions with copyright arrangements, referencing, and help with the layout. Cindy, thank you very much for your great help. One of us (H.H.) thanks the Swedish Foundation for International Cooperation in Research and High Education for a postdoctoral scholarship.

References

1. Binnig G, Quate CF, Gerber C (1986) Phys Rev Lett 56:930
2. Munz M, Cappella B, Sturm H, Geuss M, Schulz E (2003) Filler-reinforced elastomers scanning force microscopy. Springer, Berlin Heidelberg New York
3. Colton RJ, Engel A, Frommer JE, Gaub HE, Gewirth AA, Guckenberger R, Rabe J, Heckl WM, Parkinson B (1988) Procedures in scanning probe microscopies. Wiley, New York
4. Sheiko SS (2000) New developments in polymer analytics II. Springer, Berlin Heidelberg New York
5. Sarid D (1991) Scanning force microscopy: with applications to electric, magnetic and atomic forces. Oxford University Press, Oxford
6. Wiesendanger R (1994) Scanning probe microscopy and spectroscopy: methods and applications. Cambridge University Press, Cambridge
7. Magonov SNW (1996) Surface analysis with STM and AFM: experimental and theoretical aspects of image analysis. VCH, Weinheim

8. Ratner BD, Tsukruk VV (1998) ACS symposium series, vol. 694. American Chemical Society, Washington, DC
9. Tsukruk VV, Wahl KJ (1999) ACS symposium series, vol. 741. American Chemical Society, Washington, DC
10. Goh MC (1995) In: Prigogine I, Rice SA (eds) Advances in chemical physics, vol. 91. Wiley, New York
11. Hamers RJ (1996) J Phys Chem 100:13 103
12. Miles M (1997) Science 277:1845
13. Miles MJ (1994) In: Spells (ed) Advances in the characterization of solid polymers. Chapman and Hall, London, p 17
14. Frommer J (1992) Angew Chem Int Ed 31:1298
15. Cappella B, Dietler G (1999) Surf Sci Rep 34:1
16. Burnham NA, Colton RJ, Pollock HM (1993) Phys Rev Lett 70:247
17. Frisbie CD, Rozsnyai LF, Noy A, Wrighton MS, Lieber CM (1994) Science 265:2071
18. Garbassi F, Morra M, Occhiello E (2000) Polymer surfaces: From physics to technology. Wiley, New York
19. Koenig JL (1998) Microspectroscopic imaging of polymers. Oxford University Press, Oxford
20. Kirkwood JG, Buff FP (1951) J Chem Phys 19:774
21. Segeren L, Wouters MEL, Bos M, Van den Berg JWA, Vancso GJ (2002) J Chromatogr A 969:215
22. Tan ZJ, Vancso GJ (1997) Macromolecules 30:4665
23. Wendorff JH, Fischer EW (1973) Kolloid-ZuZ Polymere 251:876
24. Adamson AW, Gast AP (1997) Physical chemistry of surfaces. Wiley Interscience, New York
25. Massia SP, Hubbell JA (1991) J Cell Biol 114:1089
26. Chen CS, Mrksich M, Huang S, Whitesides GM, Ingber DE (1997) Science 276:1425
27. Maheshwari G, Brown G, Lauffenburger DA, Wells A, Griffith LG (2000) J Cell Sci 113:1677
28. Craighead HG, James CD, Turner AMP (2001) Curr Opin Solid State Mater Sci 5:177
29. Goessl A, Bowen-Pope DF, Hoffman AS (2001) J Biomed Mater Res 57:15
30. Young T (1855) In: Murray PGJ (ed) Miscellaneous works, vol. 1, London, p 418
31. Dupré A (1869) Théorie mécanique de la chaleur. Gauthier-Villars, Paris
32. Cassie ABD (1948) Discuss Faraday Soc 3:11
33. Israelachvili JN, Gee ML (1989) Langmuir 5:288
34. Laibinis PE, Whitesides GM (1992) J Am Chem Soc 114:9022
35. Schönherr H, Feng CL, Shovsky A (2003) Langmuir 19:10 843
36. Nicolau DV, Taguchi T, Taniguchi H, Yoshikawa S (1999) Langmuir 15:3845
37. Morgen H, Pritchard DJ, Cooper JM (1995) Biosens Bioelectron 10:841
38. Gallop MA, Barrett RW, Dower WJ, Fodor SPA, Gordon EM (1994) J Med Chem 37:1233
39. Fodor SPA, Read JL, Pirrung MC, Stryer L, Lu AT, Solas D (1991) Science 251:767
40. Thiebaud P, Lauer L, Knoll W, Offenhausser A (2002) Appl Surf Sci 17:87
41. Effenhauser CS, Bruin GJM, Paulus A, Ehrat M (1997) Anal Chem 69:3451
42. Makohliso SA, Leonard D, Giovangrandi L, Mathieu HJ, Ilegems M, Aebischer P (1999) Langmuir 15:2940
43. Takano H, Sul JY, Mazzanti ML, Doyle RT, Haydon PG, Porter MD (2002) Anal Chem 74:4640
44. Granlund T, Nyberg T, Roman LS, Svensson M, Inganas O (2000) Adv Mater 12:269
45. Teetsov J, Vanden Bout DA (2000) J Phys Chem B 104:9378

46. Xia YN, Whitesides GM (1998) Angew Chem Int Ed 37:551
47. Xia YN, Rogers JA, Paul KE, Whitesides GM (1999) Chem Rev 99:1823
48. Yasuda HK, Yeh YS, Fusselman S (1990) Pure Appl Chem 62:1689
49. Shenton MJ, Lovell-Hoare MC, Stevens GC (2001) J Phys D: Appl Phys 34:2754
50. Klages CP (1999) Materialwiss Werkstofftech 30:767
51. Hollahan J, Bell A (1974) Wiley, New York
52. Chan CM, Ko TM, Hiraoka H (1996) Surf Sci Rep 24:3
53. Yasuda H (1985) Plasma polymerization. Academic Press, Orlando
54. Gupta B, Anjum N (2003) Radiation effects on polymers for biological use. Springer, Berlin Heidelberg New York
55. Meek JM, Craggs JD (1978) Electrical breakdown of gases. Wiley, New York
56. Tang LP, Wu YL, Timmons RB (1998) J Biomed Mater Res 42:156
57. Schönherr H, Van Os MT, Forch R, Timmons RB, Knoll W, Vancso GJ (2000) Chem Mater 12:3689
58. Schönherr H, Hruska Z, Vancso GJ (2000) Macromolecules 33:4532
59. Ohl A, Schroder K (1999) Surf Coat Technol 119:820
60. Rossier J, Reymond F, Michel PE (2002) Electrophoresis 23:858
61. Skurat VE, Dorofeev YI (1994) Angew Makromol Chem 216:205
62. Feiertag P, Kavc T, Meyer U, Gsoels I, Kern W, Rom I, Hofer F (2001) Synth Met 121:1371
63. Vasilets VN, Nakamura K, Uyama Y, Ogata S, Ikada Y (1998) Polymer 39:2875
64. Dai LM, Griesser HJ, Hong XY, Mau AWH, Spurling TH, Yang YY, White JW (1996) Macromolecules 29:282
65. Bowden N, Brittain S, Evans AG, Hutchinson JW, Whitesides GM (1998) Nature 393:146
66. Roberts MA, Rossier JS, Bercier P, Girault H (1997) Anal Chem 69:2035
67. Lippert T, Wei J, Wokaun A, Hoogen N, Nuyken O (2000) Appl Surf Sci 168:270
68. Schwarz A, Rossier JS, Roulet E, Mermod N, Roberts MA, Girault HH (1998) Langmuir 14:5526
69. Nakayama Y, Matsuda T (1996) J Appl Phys 80:505
70. Dobisz EA, Brandow SL, Bass R, Shirey LM (1998) J Vac Sci Technol B 16:3695
71. Yasin S, Hasko DG, Ahmed H (2001) Appl Phys Lett 78:2760
72. Kim HJ, Lee KJ, Seo Y (2002) Macromolecules 35:1267
73. Berggren KK, Bard A, Wilbur JL, Gillaspy JD, Helg AG, McClelland JJ, Rolston SL, Phillips WD, Prentiss M, Whitesides GM (1995) Science 269:1255
74. Uyama Y, Kato K, Ikada Y (1998) Grafting/characterization techniques/kinetic modeling (Advances in Polymer Science), vol. 137. Springer, Berlin Heidelberg New York
75. Chapiro A (1981) EPJ 19:859
76. Ogiwara Y, Kanda M, Takumi M, Kubota H (1981) J Polym Sci, Part B:Polym Phys 19:457
77. Oster G, Shibata O (1957) J Polym Sci 26:233
78. Uchida E, Uyama Y, Ikada Y (1989) J Polym Sci, Part A: Polym Chem 27:527
79. Tazuke S, Kimura H (1978) J Polym Sci, Part B: Polym Lett 16:497
80. Zhao B, Brittain WJ (2000) Prog Polym Sci 25:677
81. Zhao B, Brittain WJ, Zhou WS, Cheng SZD (2000) J Am Chem Soc 122:2407
82. Husemann M, Morrison M, Benoit D, Frommer KJ, Mate CM, Hinsberg WD, Hedrick JL, Hawker CJ (2000) J Am Chem Soc 122:1844
83. Nakayama Y, Matsuda T (1999) Langmuir 15:5560
84. Ito Y, Chen GP, Guan YQ, Imanishi Y (1997) Langmuir 13:2756
85. Hu SW, Ren XQ, Bachman M, Sims CE, Li GP, Allbritton N (2002) Anal Chem 74:4117

86. Herminghaus S, Jacobs K, Mecke K, Bischof J, Fery A, Ibn-Elhaj M, Schlagowski S (1998) Science 282:916
87. Higgins AM, Jones RAL (2000) Nature 404:476
88. Sharp JS, Jones RAL (2002) Phys Rev E 66:11 801
89. Dalnoki-Veress K, Nickel BG, Dutcher JR (1999) Phys Rev Lett 82:1486
90. Schaffer E, Thurn-Albrecht T, Russell TP, Steiner U (2000) Nature 403:874
91. Schaffer E, Harkema S, Roerdink M, Blossey R, Steiner U (2003) Adv Mater 15:514
92. Chan CM (1994) Polymer surface modification and characterization. Hanser Gardner, München
93. Fox HW, Zisman WA (1950) J Colloid Sci 5:514
94. Fox HW, Zisman WA (1952) J Colloid Sci 7:109
95. Fox HW, Zisman WA (1952) J Colloid Sci 7:428
96. Good RJ (1964) Adv Chem Ser 43:74
97. Good RJ, Girifalco LA (1960) J Phys Chem 64:561
98. Wu S (1982) Polymer interface and adhesion. Marcel Dekker, New York
99. Wu S (1980) J Colloid Interface Sci 73:590
100. Fowkes FM (1962) J Phys Chem 66:382
101. Kaelble DH (1970) J Adhes 2:66
102. Owens DK, Wendt RC (1969) J Appl Polym Sci 13:1741
103. Van Oss CJ, Good RJ, Chaudhury MK (1986) J Colloid Interface Sci 111:378
104. Morra M, Occhiello E, Garbassi F (1990) Adv Colloid Interface Sci 32:79
105. Kloubek J (1992) Adv Colloid Interface Sci 38:99
106. Wu S, Brzozowski KJ (1971) J Colloid Interface Sci 37:686
107. Wu S (1971) J Polym Sci C34:19
108. Van Oss CJ, Chaudhury MK, Good RJ (1988) Chem Rev 88:927
109. Van Oss CJ, Chaudhury MK, Good RJ (1987) Adv Colloid Interface Sci 28:35
110. Schönherr H, Hruska Z, Vancso GJ (1998) Macromolecules 31:3679
111. Drelich J, Wilbur JL, Miller JD, Whitesides GM (1996) Langmuir 12:1913
112. Johnson REJ, Dettre RH (1964) J Phys Chem 68:1744
113. Israelachvilli JN (1991) Intermolecular and surface forces. Academic Press, London
114. Bistac S, Brogly M (2002) In: Somasundaran P (ed) Encyclopedia of surface and colloid science. Marcel Dekker, New York, p 108
115. Chen Y-L, Helm C, Israelachvilli JN (1991) J Phys Chem 95:10 736
116. Israelachvilli JN, Chen Y-L, Yoshizawa H (1995) In: Rimai DS, Demejo LP, Mittal KL (eds) Fundamentals of adhesion and interfaces. VSP, Utrecht, p 261
117. Hamaker HC (1937) Physica 4:1058
118. Rabinovich YI, Adler JJ, Ata A, Singh RK, Moudgil BM (2000) J Colloid Interface Sci 232:17
119. Johnson KL, Kendall K, Roberts AD (1971) Proc R Soc London, Ser A 324:301
120. Lifshitz EM (1995) Soviet Physics JETP-USSR 2:73
121. Schönherr H, Beulen MWJ, Bugler J, Huskens J, Van Veggel FCJM, Reinhoudt DN, Vancso GJ (2000) J Am Chem Soc 122:4963
122. Noy A, Frisbie CD, Rozsnyai LF, Wrighton MS, Lieber CM (1995) J Am Chem Soc 117:7943
123. Noy A, Sanders CH, Vezenov DV, Wong SS, Lieber CM (1998) Langmuir 14:1508
124. Vezenov DV, Noy A, Rozsnyai LF, Lieber CM (1997) J Am Chem Soc 119:2006
125. Feldman K, Tervoort T, Smith P, Spencer ND (1998) Langmuir 14:372
126. Thomas RC, Tangyunyong P, Houston JE, Michalske TA, Crooks RM (1994) J Phys Chem 98:4493

127. Thomas RC, Houston JE, Crooks RM, Kim T, Michalske TA (1995) J Am Chem Soc 117:3830
128. Akari S, Horn D, Keller H, Schrepp W (1995) Adv Mater 7:549
129. Green JBD, McDermott MT, Porter MD, Siperko LM (1995) J Phys Chem 99:10 960
130. Van der Vegte EW, Hadziioannou G (1997) J Phys Chem B 101:9563
131. Schönherr H, Vancso GJ (1997) Macromolecules 30:6391
132. Schönherr H, Vancso GJ (1998) J Polym Sci, Part B: Polym Phys 36:2483
133. McKendry R, Theoclitou ME, Abell C, Rayment T (1998) Langmuir 14:2846
134. McKendry R, Theoclitou ME, Rayment T, Abell C (1998) Nature 391:566
135. Green JBD, McDermott MT, Porter MD (1996) J Phys Chem 100:13 342
136. Noy A, Vezenov DV, Lieber CM (1997) Annu Rev Mater Sci 27:381
137. Van der Vegte EW, Hadziioannou G (1997) Langmuir 13:4357
138. Sinniah SK, Steel AB, Miller CJ, ReuttRobey JE (1996) J Am Chem Soc 118:8925
139. Weihs TP, Nawaz Z, Jarvis SP, Pethica JB (1991) Appl Phys Lett 59:3536
140. Sheiko SS, Moller M, Reuvekamp E, Zandbergen HW (1993) Phys Rev B 48:5675
141. Binggeli M, Mate CM (1994) Appl Phys Lett 65:415
142. Weisenhorn AL, Hansma PK, Albrecht TR, Quate CF (1989) Appl Phys Lett 54:2651
143. Schönherr H (1999) From Functional Group Ensembles to Single Molecules: Scanning Force Microscopy of Supramolecular and Polymeric Systems, Ph. D. Thesis, University of Twente
144. Bar G, Thomann Y, Brandsch R, Cantow HJ, Whangbo MH (1997) Langmuir 13:3807
145. Bar G, Brandsch R, Whangbo MH (1998) Langmuir 14:7343
146. Bar G, Thomann Y, Whangbo MH (1998) Langmuir 14:1219
147. Krausch G, Hipp M, Boltau M, Marti O, Mlynek J (1995) Macromolecules 28:260
148. Overney RM, Meyer E, Frommer J, Brodbeck D, Luthi R, Howald L, Guntherodt HJ, Fujihira M, Takano H, Gotoh Y (1992) Nature 359:133
149. Putman CAJ, De Grooth BG, Van Hulst NF, Greve J (1992) J Appl Phys 72:6
150. Viani MB, Schaffer TE, Chand A, Rief M, Gaub HE, Hansma PK (1999) J Appl Phys 86:2258
151. Viani MB, Schaffer TE, Paloczi GT, Pietrasanta LI, Smith BL, Thompson JB, Richter M, Rief M, Gaub HE, Plaxco KW, Cleland AN, Hansma HG, Hansma PK (1999) Rev Sci Instrum 70:4300
152. Burnham NA, Colton RJ, Pollock HM (1992) Phys Rev Lett 69:144
153. Hutter JL, Bechhoefer J (1993) Rev Sci Instrum 64:1868
154. Sader JE (1998) J Appl Phys 84:64
155. Tortonese M, Kirk M (1997) Proc SPIE 3009:53
156. Weisenhorn AL, Maivald P, Butt HJ, Hansma PK (1992) Phys Rev B 45:11 226
157. Carpick RW, Salmeron M (1997) Chem Rev 97:1163
158. Vancso GJ, Schönherr H (1999) In: Tsukruk VV, Wahl KJ (eds) Microstructure and microtribology of polymer surfaces (ACS Symposium Series), vol. 741. American Chemical Society, New York, p 317
159. Hugel T, Seitz M (2001) Macromol Rapid Commun 22:989
160. Janshoff A, Neitzert M, Oberdorfer Y, Fuchs H (2000) Angew Chem Int Ed 39:3213
161. Zapotoczny S, Auletta T, De Jong MR, Schönherr H, Huskens J, Van Veggel FCJM, Reinhoudt DN, Vancso GJ (2002) Langmuir 18:6988
162. Auletta T, De Jong MR, Mulder A, van Veggel FCJM, Huskens J, Reinhoudt DN, Zou S, Zapotoczny S, Schönherr H, Vancso GJ, Kuipers L (2004) J Am Chem Soc 126:1577
163. Jenkins ATA, Boden N, Bushby RJ, Evans SD, Knowles PF, Miles RE, Ogier SD, Schönherr H, Vancso GJ (1999) J Am Chem Soc 121:5274

164. Alley RL, Komvopoulos K, Howe RT (1994) J Appl Phys 76:5731
165. Howald L, Luthi R, Meyer E, Guthner P, Guntherodt HJ (1994) Z Phys B: Condens Matter 93:267
166. Akari S, Schrepp W, Horn D (1996) Langmuir 12:857
167. Werts MPL, Van der Vegte EW, Grayer V, Esselink E, Tsitsilianis C, Hadziioannou G (1998) Adv Mater 10:452
168. Vancso GJ, Snétivy D, Schönherr H (1998) In: Ratner BD, Tsukruk VV (eds) Scanning probe microscopy of polymers (ACS Symposium Series), vol. 694. American Chemical Society, New York, p 67
169. Vancso GJ, Förster S, Leist H (1996) Macromolecules 29:2158
170. Nisman R, Smith P, Vancso GJ (1994) Langmuir 10:1667
171. Smith PF, Nisman R, Ng C, Vancso GJ (1994) Polym Bull 33:459
172. Pearce R, Vancso GJ (1998) Polymer 39:6743
173. Mizes HA, Loh KG, Miller RJD, Ahuja SK, Grabowski EF (1991) Appl Phys Lett 59:2901
174. Joyce SA, Houston JE, Michalske TA (1992) Appl Phys Lett 60:1175
175. Van der Werf KO, Putman CAJ, De Grooth BG, Greve J (1994) Appl Phys Lett 65:1195
176. Baselt DR, Baldeschwieler JD (1994) J Appl Phys 76:33
177. Berger CEH, Van der Werf KO, Kooyman RPH, De Grooth BG, Greve J (1995) Langmuir 11:4188
178. Radmacher M, Cleveland JP, Fritz M, Hansma HG, Hansma PK (1994) Appl Surf Sci 66:2159
179. Hillborg H, Tomczak N, Olah A, Schönherr H, Vancso GJ (2004) Langmuir 20:785
180. Jaeger R, Bergshoef MM, Batlle CMI, Schönherr H, Vancso GJ (1998) Macromol Symp 127:141
181. Jaeger R, Schönherr H, Vancso GJ (1996) Macromolecules 29:7634
182. Krotil HU, Stifter T, Waschipky H, Weishaupt K, Hild S, Marti O (1999) Surf Interface Anal 27:336
183. Okabe Y, Furugori M, Tani Y, Akiba U, Fujihira M (2000) Ultramicroscopy 82:203
184. Krotil HU, Stifter T, Marti O (2000) Rev Sci Instrum 71:2765
185. Hruska Z, Lepot X (2000) J Fluorine Chem 105:87
186. Duwez AS, Nysten B (2001) Langmuir 17:8287
187. Duwez AS, Poleunis C, Bertrand P, Nysten B (2001) Langmuir 17:6351
188. Ton-That C, Teare DOH, Bradley RH (2000) Chem Mater 12:2106
189. Ton-That C, Campbell PA, Bradley RH (2000) Langmuir 16:5054
190. Eaton PJ, Graham P, Smith JR, Smart JD, Nevell TG, Tsibouklis J (2000) Langmuir 16:7887
191. Eaton P, Smith JR, Graham P, Smart JD, Nevell TG, Tsibouklis J (2002) Langmuir 18:3387
192. Nie HY, Walzak MJ, Berno B, McIntyre NS (1999) Langmuir 15:6484
193. Yip J, Chan K, Sin KM, Lau KS (2003) Appl Surf Sci 205:151
194. Wang B, Chen L, Abdulali-Kanji Z, Horton JH, Oleschuk RD (2003) Langmuir 19:9792
195. Bhargava R, Wall BG, Koenig JL (2000) Appl Spectrosc 54:470
196. Benninghoven A (1994) Angew Chem Int Ed 33:1023
197. Van Vaeck L, Adriaens A, Gijbels R (1999) Mass Spectrom Rev 18:1
198. Adriaens A, Van Vaeck L, Adams F (1999) Mass Spectrom Rev 18:48
199. Hagenhoff B (2000) Mikrochim Acta 132:259
200. Chabala JM, Soni KK, Li J, Gavrilov KL, Levisetti R (1995) Int J Mass Spectrom Ion Processes 143:191
201. Kotter F, Benninghoven A (1998) Appl Surf Sci 133:47

202. Leonard D, Mathieu HJ (1999) Fresenius J Anal Chem 365:3
203. Stapel D, Thiemann M, Benninghoven A (2000) Appl Surf Sci 158:362
204. Stapel D, Benninghoven A (2001) Appl Surf Sci 174:261
205. Hagenhoff B, Deimel M, Benninghoven A, Siegmund HU, Holtkamp D (1992) J Phys D: Appl Phys 25:818
206. Bourdos N, Kollmer F, Benninghoven A, Sieber M, Galla HJ (2000) Langmuir 16:1481
207. Frisbie CD, Wollman EW, Wrighton MS (1995) Langmuir 11:2563
208. Bernasik A, Rysz J, Budkowski A, Kowalski K, Camara J, Jedlinski J (2001) Macromol Rapid Commun 22:829
209. Bullett NA, Short RD, O'Leary T, Beck AJ, Douglas CWI, Cambray-Deakin M, Fletcher IW, Roberts A, Blomfield C (2001) Surf Interface Anal 31:1074
210. Yang ZP, Belu AM, Liebmann-Vinson A, Sugg H, Chilkoti A (2000) Langmuir 16:7482
211. Brummel CL, Lee INW, Zhou Y, Benkovic SJ, Winograd N (1994) Science 264:399
212. Brummel CL, Vickerman JC, Carr SA, Hemling ME, Roberts GD, Johnson W, Weinstock J, Gaitanopoulos D, Benkovic SJ, Winograd N (1996) Anal Chem 68:237
213. Pacholski ML, Winograd N (1999) Chem Rev 99:2977
214. Cannon DM, Pacholski ML, Winograd N, Ewing AG (2000) J Am Chem Soc 122:603
215. Belu AM, Yang ZP, Aslami R, Chilkoti A (2001) Anal Chem 73:143
216. Leufgen KM, Rulle H, Benninghoven A, Sieber M, Galla HJ (1996) Langmuir 12:1708
217. Weng LT, Smith TL, Feng JY, Chan CM (1998) Macromolecules 31:928
218. Li HW, Huck WTS (2002) Curr Opin Solid State Mater Sci 6:3
219. Quirk RA, Briggs D, Davies MC, Tendler SJB, Shakesheff KM (2001) Surf Interface Anal 31:46
220. Deimel M, Rulle H, Liebing V, Benninghoven A (1998) Appl Surf Sci 134:271
221. Gerardi C, DeRiccardis F, Milella E (1998) Mater Sci Eng, C 5:203
222. Marien J, Ghitti G, Jerome R, Teyssie P (1993) Polym Bull 30:435
223. Fulghum JE (1999) J Electron Spectrosc Relat Phenom 100:331
224. Turner NH, Schreifels JA (2000) Anal Chem 72:99R
225. Drummond IW (1996) Philos Trans R Soc London, Ser A 354:2667
226. Artyushkova K, Wall B, Koenig J, Fulghum JE (2000) Appl Spectrosc 54:1549
227. Lippert T, Ortelli E, Panitz JC, Raimondi F, Wambach J, Wei J, Wokaun A (1999) Appl Phys A 69:S651
228. Gusev AI, Vasseur OJ, Proctor A, Sharkey AG, Hercules DM (1995) Anal Chem 67:4565
229. Garden RW, Sweedler JV (2000) Anal Chem 72:30
230. Stoeckli M, Farmer TB, Caprioli RM (1999) J Am Soc Mass Spectrom 10:67
231. Krause J, Stoeckli M, Schlunegger UP (1996) Rapid Commun Mass Spectrom 10:1927
232. Tabaksblat R, Meier RJ, Kip BJ (1992) Appl Spectrosc 46:60
233. Mulvaney SP, Keating CD (2000) Anal Chem 72:145R
234. Pappas D, Smith BW, Winefordner JD (2000) Appl Spectrosc Rev 35:1
235. Keen I, Rintoul L, Fredericks PM (2001) Appl Spectrosc 55:984
236. Kagan CR, Harris TD, Harris AL, Schilling ML (1998) J Chem Phys 108:6892
237. Schaeberle MD, Morris HR, Turner JF, Treado PJ (1999) Anal Chem 71:175A
238. Appel R, Zerda TW, Waddell WH (2000) Appl Spectrosc 54:1559
239. Blakey I, George GA (2000) Polym Degrad Stab 70:269
240. Markwort L, Kip B, Dasilva E, Roussel B (1995) Appl Spectrosc 49:1411
241. Kim H, Urban MW (2000) Langmuir 16:5382
242. Zhao YQ, Urban MW (2000) Macromolecules 33:2184
243. Schmidt P, Kolarik J, Lednicky F, Dybal J, Lagaron JM, Pastor JM (2000) Polymer 41:4267

244. Morgan RL, Hill MJ, Barham PJ, Van der Pol A, Kip BJ, Ottjes R, van Ruitein J (2001) Polymer 42:2121
245. Morris HR, Munroe B, Ryntz RA, Treado PJ (1998) Langmuir 14:2426
246. Fernandez MR, Merino JC, Gobernado-Mitre MI, Pastor JM (2000) Appl Spectrosc 54:1105
247. Rossier JS, Bercier P, Schwarz A, Loridant S, Girault HH (1999) Langmuir 15:5173
248. Narita Y, Tadokoro T, Ikeda T, Saiki T, Mononobe S, Ohtsu M (1998) Appl Spectrosc 52:1141
249. Jahncke CL, Paesler MA, Hallen HD (1995) Appl Phys Lett 67:2483
250. Yang XM, Tryk DA, Hashimoto K, Fujishima A (1998) J Raman Spectrosc 29:725
251. Kneipp K, Kneipp H, Itzkan I, Dasari RR, Feld MS (1999) Chem Rev 99:2957
252. Campion A, Kambhampati P (1998) Chem Soc Rev 27:241
253. Yang XM, Tryk DA, Hasimoto K, Fujishima A (1996) Appl Phys Lett 69:4020
254. Yang XM, Tryk DA, Ajito K, Hashimoto K, Fujishima A (1996) Langmuir 12:5525
255. Teetsov JA, Vanden Bout DA (2001) J Am Chem Soc 123:3605
256. Dunn RC (1999) Chem Rev 99:2891
257. DeAro JA, Weston KD, Buratto SK, Lemmer U (1997) Chem Phys Lett 277:532
258. Stevenson R, Granstrom M, Richards D (1999) Appl Phys Lett 75:1574
259. Teetsov J, Vanden Bout DA (2001) Macromol Symp 167:153
260. Teetsov J, Vanden Bout DA (2002) Langmuir 18:897
261. DeAro JA, Moses D, Buratto SK (1999) Appl Phys Lett 75:3814
262. DeAro JA, Lemmer U, Moses D, Buratto SK (1999) Synth Met 101:300
263. DeAro JA, Gupta R, Heeger AJ, Buratto SK (1999) Synth Met 102:865
264. Nguyen TQ, Martini IB, Liu J, Schwartz BJ (2000) J Phys Chem B 104:237
265. Nguyen TQ, Schwartz BJ, Schaller RD, Johnson JC, Lee LF, Haber LH, Saykally RJ (2001) J Phys Chem B 105:5153
266. Huser T, Yan M (2001) Synth Met 116:333
267. Kwak ES, Kang TJ, Bout DAV (2001) Anal Chem 73:3257
268. Dragnea B, Preusser J, Szarko JM, McDonough LA, Leone SR, Hinsberg WD (2001) Appl Surf Sci 175:783
269. Dragnea B, Preusser J, Schade W, Leone SR, Hinsberg WD (1999) J Appl Phys 86:2795

Editor: Hans-Henning Kausch